

REVIEW ARTICLE

SEM, FTIR and TGA analysis of Graphitic carbon nitride (g-C₃N₄) and its modification as a composite material

Karel Klouda^{1,2}, Petra Roupcová^{1*}, Petra Bursíková³, Romana Friedrichová³, Kateřina Bátorlová², Eva Kuželová Košťáková⁴, Zdeněk Starý⁵, Jiří Tílhon²

¹ VSB – Technical University of Ostrava, Faculty of Safety Engineering; klouda@vubp.cz; petra.roupcova@vsb.cz

² Research Institute for Labour and Social Affairs; klouda@rilsa.cz; batrlova@rilsa.cz; tilhon@rilsa.cz

³ Technical Institute of Fire Protection, Ministry of the Interior – General Directorate of Fire Rescue Service of the Czech Republic; petra.bursikova@hzscr.cz; romana.friedrichova@hzscr.cz

⁴ Technical University of Liberec; eva.kostakova@tul.cz

⁵ Institute of Macromolecular Chemistry, Czech Academy of Sciences; stary@imc.cas.cz

*Corresponding author: Petra Roupcová, petra.roupcova@vsb.cz

ABSTRACT

This paper describes the preparation of g-C₃N₄ by polycondensation of melamine at 511 °C and its subsequent doping with Fe₂O₃, Cu, GO, rGO, DA and their combinations. Graphitic carbon nitride represents an innovative material with numerous applications, particularly within the domains of catalysis and water treatment. FTIR and thermogravimetric analysis were predominantly employed for the purpose of identification, while SEM images were captured at incremental resolutions. The subsequent section of the manuscript delineates the fabrication of composite materials within polymers, including PE-foil and PP-filaments intended for 3D printing, as well as PVB into nanofibers via electrostatic spinning techniques. The objective of this study was to examine the thermal stability of nanofibers produced from PVB in conjunction with g-C₃N₄ composite (18-20 %) utilizing two methodologies: EL DC spinning and EL AC spinning. The material exhibiting the most efficacious synthesis will undergo further assessment to evaluate its potential utility in the photocatalytic degradation of environmental pollutants.

Keywords: graphitic carbon nitride; doping of materials; melamine; polymer materials; degradation of pollutants

ARTICLE INFO

Received: 14 March 2025

Accepted: 01 April 2025

Available online: 25 June 2025

COPYRIGHT

Copyright © 2025 by author(s).

Applied Chemical Engineering is published by Arts and Science Press Pte. Ltd. This work is licensed under the Creative Commons Attribution-NonCommercial 4.0 International License (CC BY 4.0).

<https://creativecommons.org/licenses/by/4.0/>

1. Introduction

It is a substance that is prepared by thermal polycondensation at a temperature of 450–660 °C^[1] from nitrogen-rich precursors with C-N core structure such as melamine, cyanamide, dicyandiamide, urea, thiourea; see scheme in **Figure 1**.

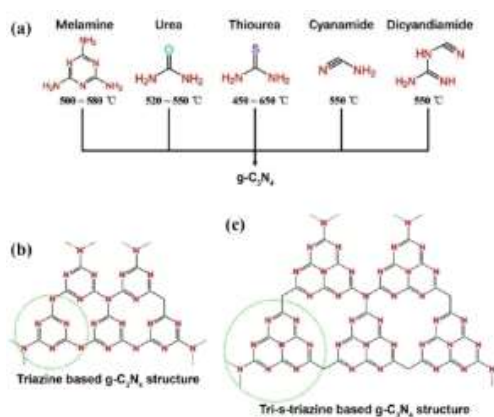
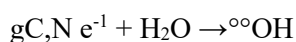


Figure 1. Initial precursors of the synthesis process of g-C₃N₄, structures of nanosheets.

With a graphite-like layered structure, g-C₃N₄ is in a form of 2D nanosheets, based on s-triazine or tri-s-triazine (**Figure 1**) tectonic unit interconnected via tertiary amines^[2]. The presence of sp²-hybridized C and N results in the unique g-C₃N₄, which plays a prime role in photocatalytic technologies, it is a highly active non-metallic photocatalyst^[3]. The photocatalytic activities of g-C₃N₄ are considerably affected by its structure, including its electronic structure. Both doping and composites are used for influence to obtain improved properties of new compounds, which then allow a wide range of possibilities for adaptive properties, e.g. for photocatalytic degradation, environmental remediation, removal of heavy metals from contaminated water, photocatalytic water splitting, photoreduction of CO₂, etc. Another factor is the influence of micro-, meso- and macro-pores in the fabric. Pore size influences water decomposition, production of H₂ and O₂, reduction of CO₂ (CH₃OH, CH₄). HARD-TEMPLATE METHOD, SOFT-TEMPLATE METHOD and TEMPLATE-FREE METHOD are also described. These methods modify the pore structure. g-C₃N₄ can be exfoliated chemically, mechanically and by ultrasound^[4-6]. An important application of g-C₃N₄ is in wastewater treatment by photo-oxidation reactions, where organic pollutants are degraded, bacteria are inactivated, and toxic heavy metals, antibiotics and a range of organic compounds are removed by photo-reduction reaction^[7-10]. One of the other applications of g-C₃N₄ is membrane formation, which is used to trap pollutants, phenols, pharmaceutical products, organic dyes, and for desalination. g-C₃N₄ shows good photocatalytic activity under visible light^[11-13].



Graphitic carbon nitride can be functionalized^[14] –COOH, –SO₃H, –OH to affect the electrochemical and physicochemical properties by elemental doping, both non-metallic (S, O, B, Cl, F) and metallic (Fe, Ni, Pb, Ag, Au). Applications in supercapacitors, in photocatalytic water splitting, as a flame retardant, appear to be promising^[15,16]. g-C₃N₄ is one of the photocatalysts with minimal toxicity, a chemically stable substance with efficient light absorption in the visible near-infrared region^[17,18].

The novelty of this study lies in the synthesis and structural modification of g-C₃N₄ through its integration with various polymer matrices (PP, PE, LDPE, PVB), followed by a comprehensive comparative analysis using selected techniques. Unlike previous studies that focus primarily on g-C₃N₄ as a standalone photocatalyst, this work explores its behavior within composite systems, aiming to enhance its thermal stability and structural adaptability for future photocatalytic applications. Furthermore, the study proposes a novel direction for testing photocatalytic activity under magnetic fields in the absence of light, which has not been widely investigated in current literature.

The aim of this article was to synthesize g-C₃N₄ and its modifications with diverse materials and to implement these modifications within a composite framework with polymer materials. The synthesized products were subsequently subjected to FTIR, SEM, and TGA analyses to facilitate comparative evaluation and further examination of their properties.

2. Materials and methods

2.1. Materials

Chemicals:

- Melamine – purity 99 %; CAS: 108-78-1; Sigma-Aldrich s.r.o.;
- Low Density Polyethylene (LDPE) TYPE 100 BW Exxon Mobil;
- Polyvinyl butyral (PVB), Mowital, Kuraray Europe GmnH; Germany;
- Dopamine hydrochloride – PA; CAS: 62-31-7; Sigma-Aldrich s.r.o.;

- Tris (hydroxymethyl) amino- methane; purity 99,8 %; Sigma-Aldrich s.r.o.; CAS: 77-86-1;
- Iron oxide - nanoscale –purity 96 %; CAS:1309-37-1; Sigma-Aldrich s.r.o.;
- Graphene oxide (GO)– preparation by Hummers’ method^[19];
- Reduced graphene oxide (rGO) – reduced by ascorbic acid^[19];
- Graphene oxide MEND (GO MEND) – provided by the Mendel University in Brno in suspension 2gL⁻¹ ^[20].

2.2. Methods

- **FTIR spectroscopy** (Nicolet iS20 FTIR Spectrometer: type of experiment: single reflection diamond ATR; sample preparation: solid samples measured directly; powdered samples ground into a fine powder; the spectra were not modified using any corrections; measurement conditions: the spectral resolution: 4 cm⁻¹; the number of scans: 128; technical parameters of the device:
 - detector: thermoelectrically cooled DTGS;
 - IR source: single-point IR ceramic;
 - laser: solid-state, temperature-controlled diode laser;
 - beamsplitter: KBr;
 - Spectral range: 7800 – 350 cm⁻¹;
 - Omnic 9 software.
- **SEM EDX spectroscopy:** (Tescan Vega 4, Tescan Vega 3) with accelerating voltage 15 keV.
- **Thermogravimetric analysis** (STA 449 F3 JUPITER DTA): air atmosphere, flow rate is 40 ml/min, temperature range is from 30 °C to 750 °C, speed heating is 20 °C/min.
- **Other instruments:**
 - Electric furnace 018LP fg Svoboda;
 - Mini extruder Mini CTW Haace;
 - Hydraulic press FONTIJNE.

2.3. Preparation of g-C₃N₄

The synthesis is achieved through the thermal polycondensation of melamine. The melamine powder was deposited onto a substrate of aluminum foil and subsequently introduced into an electric furnace. The elevation to the reaction temperature of 511 °C from an initial temperature of 19 °C required a duration of one hour. The polycondensation process at this specified temperature continued for a period of 4 hours. Following the cessation of the furnace operation, it underwent a cooling period of approximately 2 hours, resulting in the acquisition of 4.12 g of the yellow product g-C₃N₄ (20% yield).

2.4. Subsequent reactions of g-C₃N₄

a) Reactions with dopamine hydrochloride

g-C₃N₄ (2.8 g) + 30 ml of 50% C₂H₅OH was alternately mixed and sonicated for about 30 minutes. Subsequently, a solution of DA·HCl (1.4 g) in 30 ml of distilled water with 30% H₂O₃ (15 ml) was added and modified in TRIS to pH 8.5. The reaction mixture was mixed at laboratory temperature for 16 hours and then filtered and dried at a temperature of 55 °C. (point a)

b) Reaction with graphene oxide (GO)

Together in aqueous medium, the mixture of g-C₃N₄ (1.1 g) with GO (1.0 g) was alternately mixed and sonicated for 16 hours, then the mixture was filtered and dried at a temperature of 55 °C.

c) Reaction with reduced graphene oxide rGO

This reaction followed the same reaction pathway as in point a)

d) Reaction with iron nano-oxide without and after addition of GO

| | | | | | |
|---------------------------------|----------|---|--------------------------------|----------|--|
| g-C ₃ N ₄ | (3.85 g) | 30 ml C ₂ H ₅ OH ₈ | C ₃ N ₄ | (3.85 g) | 30 ml C ₂ H ₅ OH |
| Fe ₂ O ₃ | (1 g) | | Fe ₂ O ₃ | (1 g) | |
| | | | GO | (2 g) | 15 ml C ₂ H ₅ OH |

e) Reaction with iron nano-oxide after addition of (DA) dopamine hydrochloride

| | | |
|---|--|--|
| g-C ₃ N ₄ | | 30 ml C ₂ H ₅ OH ₈ |
| Fe ₂ O ₃ (5,39 g) | | mixed and sonicated for 30 minutes |
| DA·HCl (1.4 g) | | 40 ml H ₂ O + 15 ml H ₂ O ₃ (50%) |
| TRIS pH 8.5 | | |

It was mixed at laboratory temperature for 16 hours and then the reaction mixture was filtered and dried at a temperature of 55 °C.

Mixtures of g-C₃N₄ with ethanol were magnetically mixed side by side in Erlenmeyer flasks for 15 minutes; without mixing they were placed in a sonication bath. This run for 1 hour and graphene oxide was added to the second flask. The sonication bath was heated to 40–50 °C. The alternating procedure of mixing and sonication took 2 hours. Both reactions were then mixed at a temperature of 21 °C overnight (16 hours). Filtration followed, the cake was washed with C₂H₅OH and distilled water and then the filter cake was allowed to dry at a temperature of 55 °C.

f) Thermal reaction with graphene oxide in the presence of hydrogen peroxide

Together in aqueous medium (20 ml of H₂O), the mixture of g-C₃N₄ (1.0 g) with GO (1.0 g) was alternately mixed and sonicated for 1 hour. Subsequently, the reaction flask containing this mixture was placed in a water bath (70–80 °C) and hydrogen peroxide (30%) was added in an amount of 35 ml and the flask was closed with a plastic stopper. The flask was left in this water bath for 2 hours. The contents of the flask were then filtered and the filtered product was dried.

g) Reactions with graphene oxide provided by the Mendel University in Brno (GO-MEND)

g-C₃N₄ (1 g) + 7 ml of C₂H₅OH sonicated for 30 minutes, then 12 ml of GO suspension were added. Alternately mixed (shaken) and sonicated (40–50 °C) for 2 hours (the mixture was grey in colour). Subsequently, the suspension was poured onto PVDF with one side laminated with PP. PVDF was a non-woven fabric prepared by electrospinning. The plastic sample was spherical in shape and was placed in Petri dish. The rest of the suspension was poured onto conventional filter paper and then the suspension was spontaneously evaporated. The suspension on the plastic substrate was placed in a 50 °C oven. The next day – the result was not a film as when the aqueous GO-MEND suspension itself was dried. The result was a grey-yellow powder (**Figure 3**) that did not adhere to the substrate, either on the plastic, nanofibers or filter paper. When the weight-to-weight ratio of g-C₃N₄ to GO was reduced (0.004 g, 0.004 g of GO-MEND in 2 ml of suspension), a cracked film was obtained, but it adhered to the polymer substrate, see **Figure 4**.

h) Presence of nano iron oxide in the melting of melamine

The polycondensation of melamine was repeated with weights of about 20 g of melamine with approximately 20% yield of C₃N₄. The melting process was carried out in the presence of 10% nano iron oxide

relative to melamine. After one hour, a temperature of 511 °C was reached and the reaction was held at this temperature for 2.5 hours. After opening the furnace, no common substance of g-C₃N₄ was found as it was repeatedly found in polycondensation of melamine itself; only a red-brown powder was found. Its weight corresponded in essence to the initial weight of Fe₂O₃.

The experiment was repeated with weights of 25.26 g of melamine with 1.75 Fe₂O₃, i.e. 7% relative to melamine. Temperature and time remained the same. The result was also the same - Fe₂O₃ powder in essence with the initial weight of approximately 1.66 g.

i) Presence of graphene oxide in the melting of melamine

The melting process was carried out – polycondensation of melamine together with GO, weights: melamine 26.3 g, GO 1.0 g. The mixture was mixed and placed in a furnace at 511°C for one hour until the specified temperature was reached, and then the temperature was held for 2.5 hours. After opening the furnace, some blackening of the furnace with carbon black was found; despite this finding, samples were taken for FTIR analysis and SEM acquisition.

j) Reaction with DA in the presence of Cu²⁺ and Fe

g-C₃N₄ (2.6 g) was sonicated in 25 ml of distilled water for 0.5 hour, then the reaction flask was magnetically mixed with Fe-screw and an aqueous solution of 6.02 g CuSO₄·7H₂O in 30 ml H₂O was added. The prepared mixture was mixed for 0.5 hour and then a solution of 3.02 g dopamine hydrochloride in 25 ml H₂O with TRIS and 5.5 ml H₂O₂ was added. Upon addition of dopamine, the reaction mixture turned brown and spontaneously heated to approximately 80 °C. The flask with this reaction mixture was mixed for 1 hour and then left at room temperature overnight. The solid product was filtered and dried. The filtrate obtained was a brown-black product with a weight of 2.8 g.

k) Reaction with CuSO₄·5H₂O (Cu²⁺) and Fe (VRUT) solution

The procedure was similar to that in point h) except for the part of the reaction where dopamine hydrochloride solution was added.

2.5. Preparation and identification of polymer composites film with polyethylene (g-C₃N₄, g-C₃N₄-PDA)

Low density polyethylene (LDPE) was used as the matrix for the preparation of the composite. The composite containing 10 wt% g-C₃N₄ (or 10 wt% g-C₃N₄-PDA) was prepared by mixing in melt on a mini-extruder. Mixing was carried out at a temperature of 190 °C and a screw speed of 60 min⁻¹ for one minute. The composite material thus obtained was subsequently transferred to a Fontijne hydraulic press, where 0.5 mm thick films were pressed at a temperature of 190 °C.

2.6. Preparation of filaments and their application in 3D printing – to be added

The composite material for the preparation of the printing filaments was prepared by mixing in melt using a Brabender Plasticorder W50 EH mixer at 190 °C with a rotor speed of 60 rpm. The mixing time was 8 minutes. The polypropylene homopolymer (PP) Moplen HP501L (LyondellBasell) was used as the matrix for the preparation of the composite. The content of g-C₃N₄ in the composite was 10 wt%. After granulation, the material was extruded at a temperature of 190 °C through a capillary nozzle with a diameter of 1.6 mm and aspect ratio L/D=12. The resulting printing filament had a diameter of 1.7 mm, see **Figure 2**.



Figure 2. PP-g-C₃N₄ filament samples.

2.7. Nanofibers prepared by DC and AC electrospinning

Electrospinning is currently considered to be the simplest technology for producing fibers with precisely defined properties ^[21], which uses a solution or melt and which is simultaneously based on and uses an electrostatic field during production ^[22, 23]. Fiber formation using a combination of electrostatic field and other forces is the goal of modern efforts to increase the range of electrospinning manufacturing options. Examples of this include the use of low frequencies ^[24], high frequencies ^[25] or air blowing ^[26]. However, another study ^[27] has shown that a static direct current (DC) high voltage source can be replaced by dynamic AC power, with significant productivity gains. The differences between the different approaches to the use of AC or DC electrospinning can be summarised as follows: The use of a dynamic AC voltage leads to a several-fold increase in productivity (using the same device) compared to DC voltage in the case of multiple fluid streams that are ejected from a continuously charged and discharged droplet – thus the AC being more permeable ^[27, 28]. Operation without collector. The motion of the flying nanofibre plough produced by AC voltage electrospinning is not affected by the ground potential but by the electric field surrounding the spinneret. This means that it is not necessary to have a grounded collector. When producing fibers in a confined environment (e.g., pharmaceutical manufacturing), collection is more efficient if the problem of fiber stickiness that occurs with DCES on grounded surfaces (i.e., almost all surfaces except the charged spinneret) is eliminated ^[29]. Fibre production. Fiber materials are key ingredients for other high-value three-dimensional applications such as tissue engineering or composites. However, their fabrication using the commonly used DCES method is difficult due to the occurrence of repulsion between the flying fibers ^[30]. In contrast, using AC electrospinning, twisted yarns can be easily produced without complex collection problems ^[27, 31, 32].

Various factors affecting the process. In addition to the key factors that affect DCES (e.g. polymer concentration, electric field strength, etc.), there are other possibilities such as adjusting the frequency and shape of the AC voltage waveform. These changes could be used to optimize the ACES process, for example, in terms of productivity or morphology of the resulting fibers ^[29].

A paper has been published ^[33] where g-C₃N₄ was incorporated by electrospinning into PVDF fibers in order to prepare a membrane for use in the photocatalytic degradation of pollutants (the experiment was

executed on Rhodamine B) and subsequently another experiment has been published by essentially the same authors [20], where g-C₃N₄ was doped into fibers with graphene oxide in a similar manner as described in this publication. Introduction of g-C₃N₄ as a composite into PVB nanofibers by electrospinning was done at TUL.

a) DC electrospinning - Nanospider™ (Elmarco, CZ)

Sample 1.0, see **Figure 27**, control sample – polyvinyl butyral (PVB, B60H, Kuraray), 10 wt% PVB solution in ethanol. Electrospinning - Nanospider™ – electric voltage on spinning electrode +30 kV; electric voltage on collector -10 kV; electrode spacing 200 mm; diameter of the dosing device 0.7 mm; travel speed of the dosing device 1 sec/50 cm; relative humidity 40%; temperature 22°C; substrate material - spunbond-type non-woven fabric 30 g/m² (PFNonwovens, CZ); substrate material removal rate 20 mm/min.

Sample 1.1, see **Figure 28**, - 10 wt% PVB in ethanol with the addition of 20 wt% g-C₃N₄ from dry matter of the polymer. The final theoretical concentration is 16.67 wt% g-C₃N₄ from dry matter of the resulting fibers. The formation of the solution was in the following procedure: weighing a quantity of ethanol, adding g-C₃N₄ powder crushed into smaller particles in a mortar grinder, sonication by ultrasonic homogenizer 5x10 sec; adding PVB, mixing on a magnetic mixer for 8 hours. Electrospinning - Nanospider™ – electric voltage on spinning electrode +30 kV; electric voltage on collector -10 kV; electrode spacing 200 mm; diameter of the dosing device 0.7 mm; travel speed of the dosing device 1 sec/50 cm; relative humidity 40%; temperature 22°C; substrate material - spunbond-type non-woven fabric 30 gm⁻² (PFNonwovens, CZ), see **Figure 29**; substrate material removal rate 20 mm/min.

b) AC electrospinning – rod electrode (TUL)

Sample 2.1, see **Figure 29** – AC electrospinning was carried out on equipment developed by the TUL FP and FS team. The spinning process took place under the following conditions: Effective voltage U_{ef} 35 kV; sine wave signal; frequency 50 Hz; distance of the black paper (electrically inactive collector) from the rod spinning electrode 350 mm; relative humidity 40%; temperature 22°C.

3. Results and discussion

3.1. g-C₃N₄ with dopants

3.1.1. FTIR analysis

Most of the experiments were focused on the doping of g-C₃N₄, mostly at laboratory temperature (mean value 21°C). Iron oxide powder in microscale, GO (FTIR presented in **Figure 4**), rGO (FTIR presented in **Figure 4**), copper in the native state obtained according to the principle of electrochemical series of metals, Beketov's series, i.e. copper salt and Fe-VRUT (FTIR presented in **Figure 5**) were used as doping agents. In some experiments, dopamine hydrochloride was used, which was polymerized in the reaction to polydopamine, which has adhesive abilities and the formed layer has catechol and amino functional groups on the surface.

Slightly increased reaction temperature was used during the reaction of GO in a hydrogen peroxide environment; this was to modify GO to so-called holey graphene oxide (HGO) during the reaction of g-C₃N₄ (FTIR presented in **Figure 4**)

FTIR analysis was carried out on selected products of the g-C₃N₄ reaction and SEM images were taken at different resolutions. Thermal analysis was carried out and evaluated on the products from reaction 1.3.d.

All acquired spectra are characterized by two regions, namely at 2800 cm⁻¹ and then a forest of peaks in the range 1600-500 cm⁻¹, where there are vibrations of CN – heterocycles. A more detailed description of the spectra is given under **Figure 3**. In all prepared products, a wavenumber of 808 cm⁻¹ is identified, which is interpreted as a triazine ring vibration in accordance with the reference [33].

For the products with GO, the FTIR shows a characteristic peak C=O 1637 cm⁻¹.

FTIR analysis was carried out for the initial graphitic carbon g-C₃N₄ to determine the characteristic bands and these were compared with the bands of g-C₃N₄ + Fe₂O₃ and g-C₃N₄ + Fe₂O₃ + GO (**Figure 3**).

In addition to the main preparation of g-C₃N₄, the melting of melamine in an electric furnace was tested together with Fe₂O₃ and with GO at the same temperature. In the case of melting with Fe₂O₃, the reaction found in thermal analysis was confirmed, where g-C₃N₄ decomposes in the presence of Fe₂O₃. In the case of GO, the melting temperature is approximately identical to the temperature at which the second exothermic effect takes place for GO. The obtained product visually resembles a mixture of carbon black and g-C₃N₄ and identification by FTIR, see **Figure 5**.

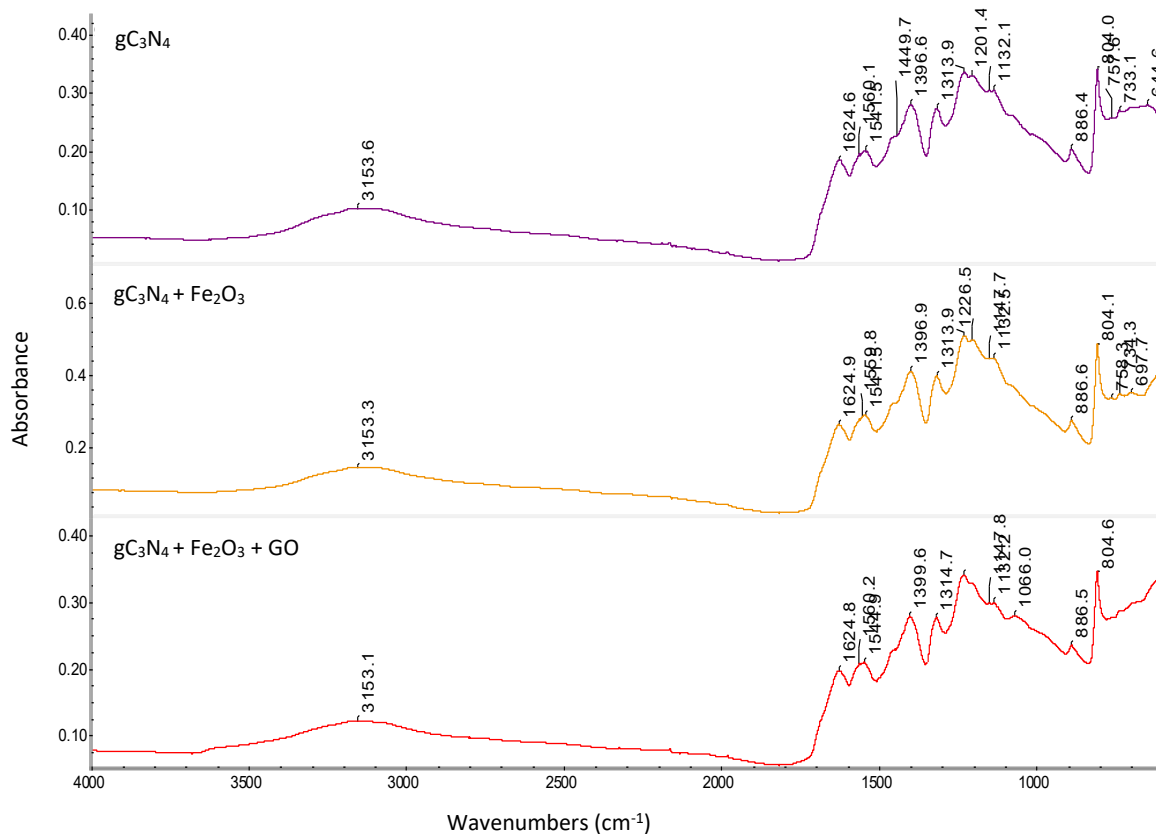


Figure 3. Comparison of FTIR spectra g-C₃N₄, g-C₃N₄ + Fe₂O₃ and g-C₃N₄ + Fe₂O₃ + GO samples with determination of characteristic bands.

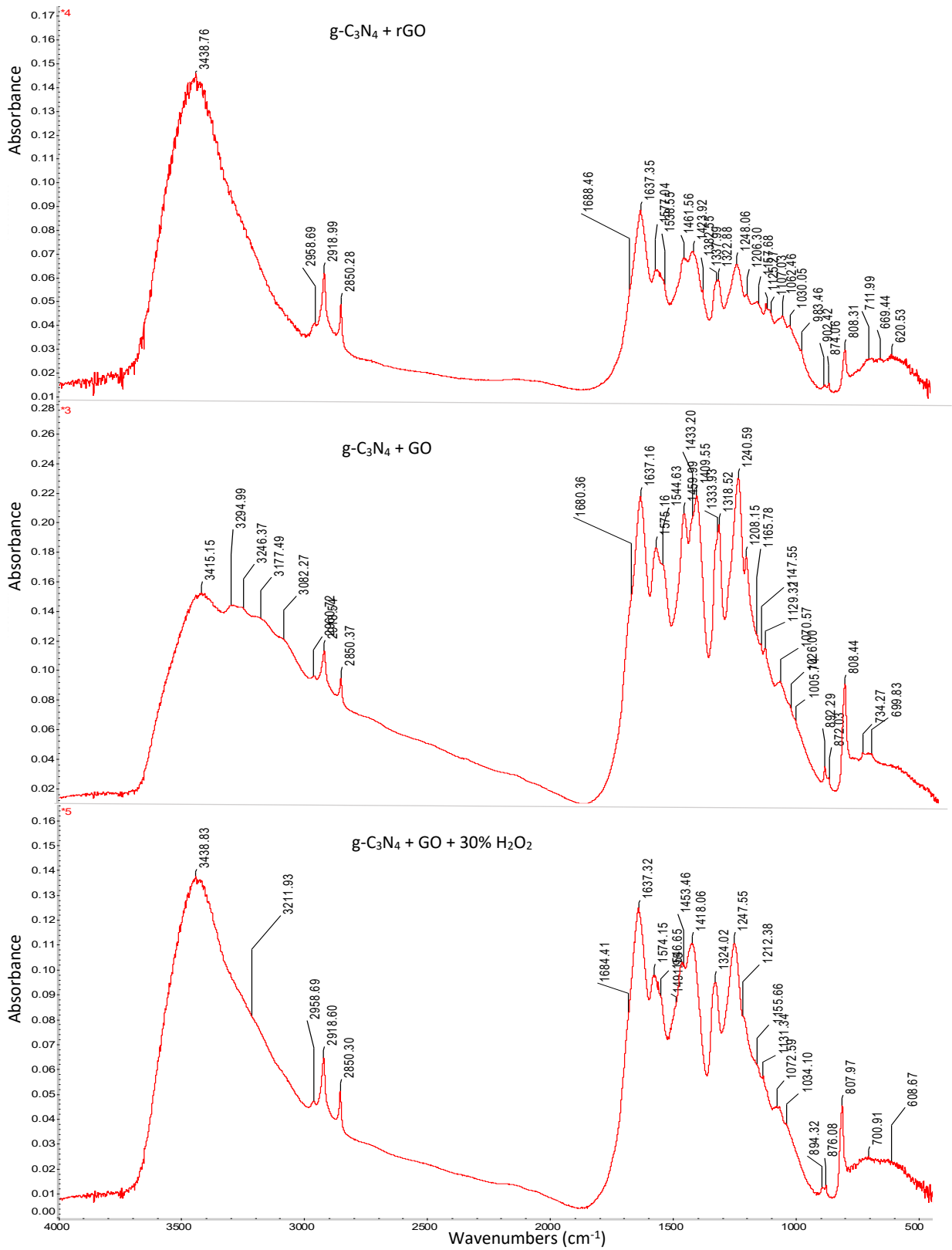


Figure 4. FTIR spectra of g-C₃N₄ + rGO, g-C₃N₄ + GO and g-C₃N₄ + GO + 30% H₂O₂.

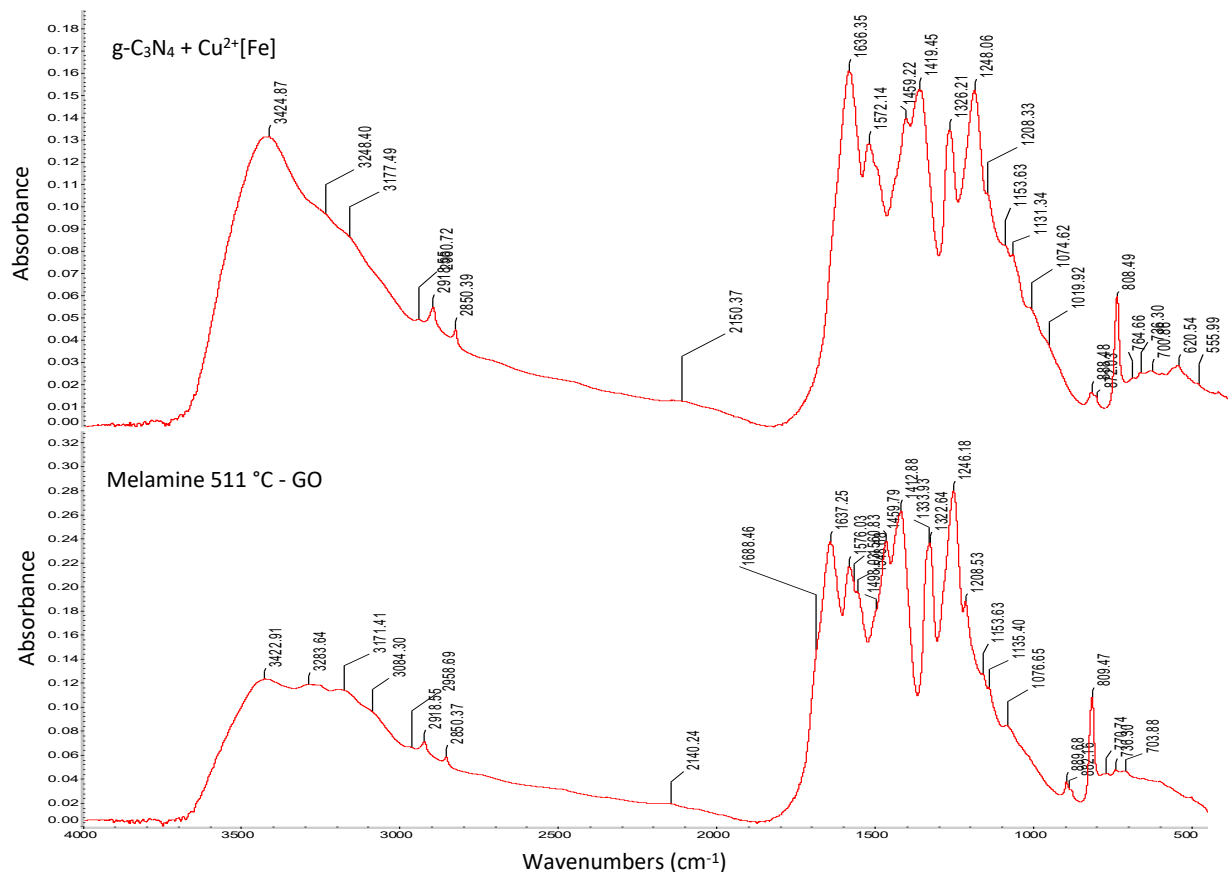


Figure 5. FTIR spectra of $C_3N_4 + Cu^{2+}[Fe]$ and melamine 511 °C -GO.

The spectra show characteristic bands that are practically the same for all measured samples. Based on the triazine-based structure, we can conclude that we are looking for C-N, C=N, CN cycle vibrations and probably also NH_2 .

- wide band 3600-2700 cm^{-1} vibration NH_2
- 1625-1540 cm^{-1} vibration C=N
- 1460-1200 cm^{-1} vibration C-N
- 1148 and 1132 cm^{-1} vibration CNC
- 805 cm^{-1} vibration of CN cycle

3.1.2. SEM analysis

The microstructure of sample $g-C_3N_4$ is presented in **Figure 6**. The lowest magnification (A) shows occurrence of aggregates randomly distributed at the observed surface. The higher magnification (B) shows that the aggregates are formed by the particles of different size and shape of porous structure. The closer analysis (C) reveals occurrence of plate-like particles (from approx. 1 μm to 5 μm) surrounded by the smaller, irregular, closely packed crystals.

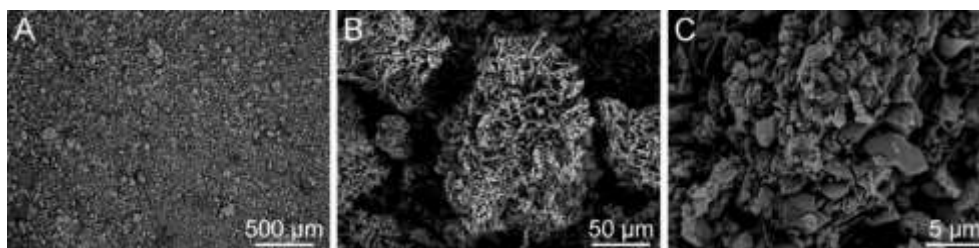


Figure 6. SEM micrographs of g-C₃N₄, SEM: SE+BSE.

The microstructure of g-C₃N₄ + Fe₂O₃ is presented in **Figure 7**. The images (A) and (B) reveal the occurrence of the aggregates that show visible porous, sponge-like surface. The higher magnification shows that the aggregates are composed of bigger, rounded plates (approx. 6 μm, the grey structures). The visible white sphere-like components are connected to the Fe₂O₃. The spheres partially cover the g-C₃N₄ surface forming the aggregates of different size up to 500 nm. The size of the single sphere-like particle is approx. 200 nm.

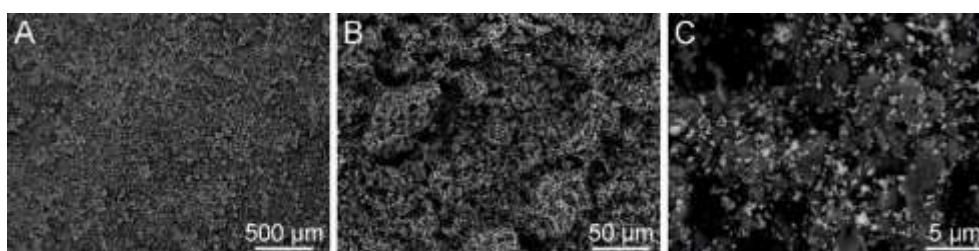


Figure 7. SEM analysis of g-C₃N₄ + Fe₂O₃, SEM: SE+BSE.

The microstructure of sample g-C₃N₄ + Fe₂O₃ + GO is presented in **Figure 8**. The surface of sample resembles the structure observed for the g-C₃N₄ (**Figure 6**). The micrographs (A) and (B) show visible porous materials composed of plates with defined sharp edges (C). The estimated size of plates is in a range of 6–7 μm. In comparison to sample g-C₃N₄, the plates observed for g-C₃N₄ + Fe₂O₃ + GO are not surrounded by smaller stacked crystals. The visible white sphere-like structures (Fe₂O₃) are similar like for sample g-C₃N₄ + Fe₂O₃ (**Figure 7**). However, the observed aggregates of spheres are visibly larger, up to 2 μm.

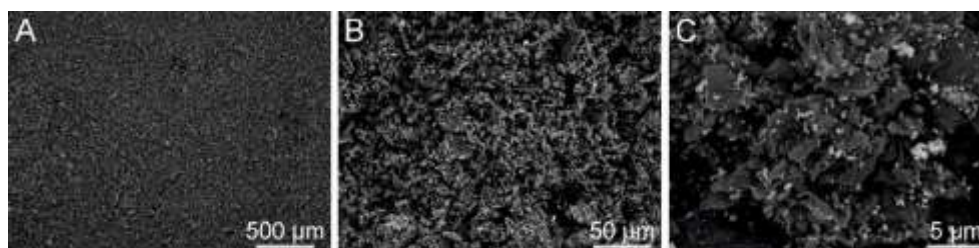


Figure 8. SEM analysis of g-C₃N₄ + Fe₂O₃ + GO, SEM: SE+BSE (Tescan Vega 4).

The microstructure of g-C₃N₄ + rGO is presented in **Figure 9**. The micrographs (A) and (B) show formation of aggregates of porous structures. The highest magnification (C) shows that the aggregates are composed of crystals of different size and shape. The bigger, coarse particles of size approx. 8 μm are surrounded by smaller plate-like particles stacked and closely packed in layers. The micrographs reveal also occurrence of elongated tube-like crystals of length approx. 5 μm

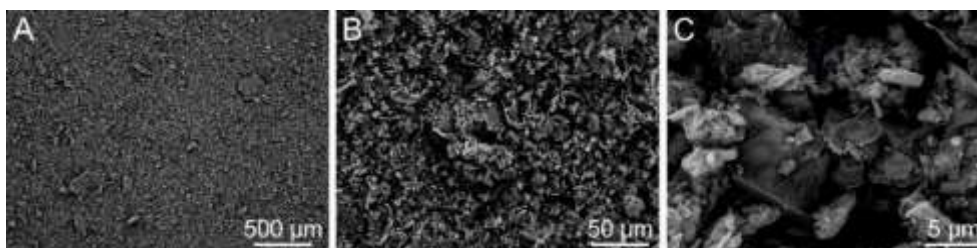


Figure 9. SEM analysis of g-C₃N₄ + rGO, SEM: SE+BSE.

The microstructure of g-C₃N₄ + GO is presented in **Figure 10**. The micrographs show occurrence of big aggregates (A) that at higher magnification (B) resembles the tree bark. The image shows formation of the ‘base’ structures – big solid particles, covered by smaller structures of undefined shape and of visibly higher porosity. The size of ‘base’ particles (C) is estimated to approx. 21–22 μm, while the smaller ‘covering’ particle size (C) is approx. 2.5–3 μm.

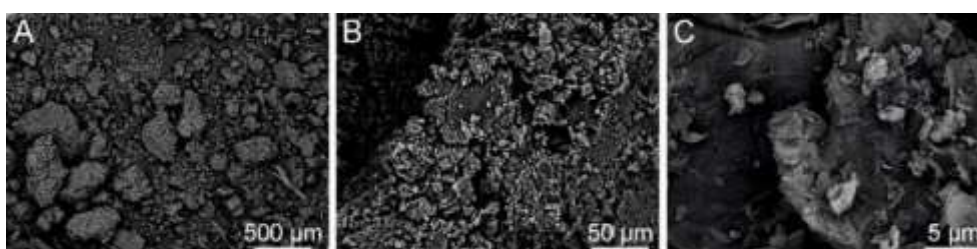


Figure 10. SEM analysis of g-C₃N₄ + GO, SEM: SE+BSE.

The microstructure of g-C₃N₄ + GO + 30% H₂O₂ is shown in **Figure 11**. The analysis of micrographs (A) and (B) shows formation of aggregates of different size. The particles observed at higher magnifications do not resemble the structures observed for previously described materials. The shape of particles is hard to define – some of the structures resemble a round-edged, deformed blocks, while other particles seem to be composed of closely packed, rounded plates. The estimated size of particles is approx. 2–5 μm.

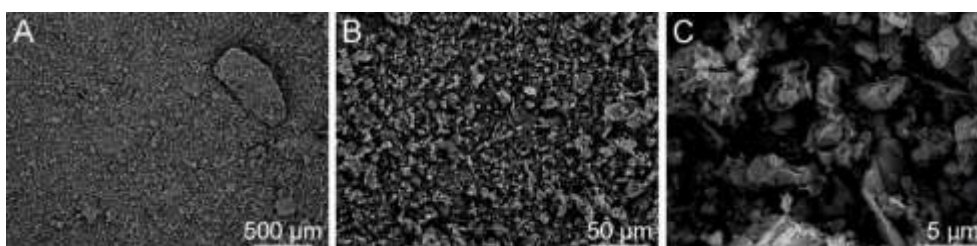


Figure 11. SEM analysis of g-C₃N₄ + GO + 30% H₂O₂, SEM: SE+BSE.

The microstructure of g-C₃N₄ + Cu²⁺[Fe] is presented in **Figure 12**. The micrographs (A) and (B) show formation of aggregates of different shape and size. The lighter particles composed of sphere-like crystals are most probably related to Fe. The highest magnification (C) allows to observe the formation of needle-like aggregates, characteristic for CuO. The micrographs do not show occurrence of plates, either rounded or sharp. The irregular blocks of size approx. 12 μm are covered by smaller formations. The estimated size of Fe related particles is approx. 500 nm (single sphere), while the aggregates of Fe are up to 4–5 μm. The length of CuO needles is approx. 500 nm.

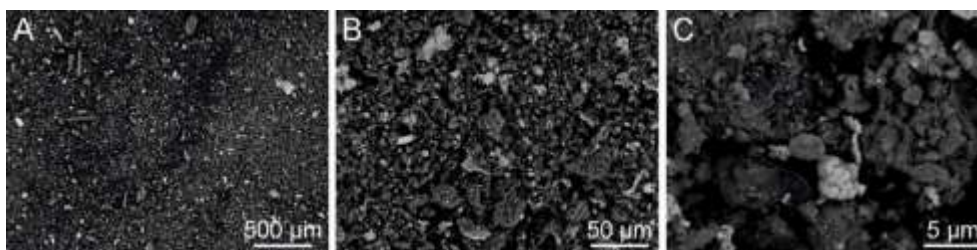


Figure 12. SEM analysis of g-C₃N₄ + Cu²⁺[Fe], SEM: SE+BSE.

The microstructure of melamine 511°C - GO is presented in **Figure 13**. The micrographs (A) and (B) show the sponge-like structure with visible porosity. The highest magnification (C) shows the solid particle composed of several closely stacked layers. The determination of size of individual plates/layers is impossible.

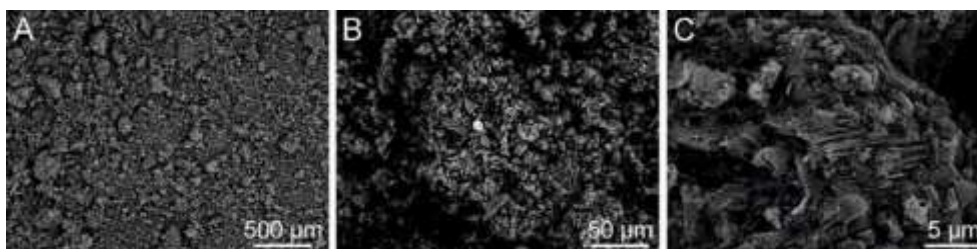


Figure 13. SEM analysis of melamine 511°C - GO, SEM: SE+BSE

3.1.3. TGA analysis

The result of thermogravimetric analysis of these products compared to the initial g-C₃N₄ was interesting. This showed the exothermic effect associated with the decomposition of the g-C₃N₄ molecule in the presence of Fe₂O₃ at temperatures around 600°C (**Figure 14, 15**). The carbon nitride itself is in essence stable at this temperature, decomposing with endothermic effect, weight units in %, **Figure 16**. In addition to the main preparation of g-C₃N₄, the melting of melamine in an electric furnace was tested together with Fe₂O₃ and with GO at the same temperature. In the case of melting with Fe₂O₃, the reaction found in thermal analysis was confirmed, where g-C₃N₄ decomposes in the presence of Fe₂O₃. In the case of GO, the melting temperature is approximately identical to the temperature at which the second exothermic effect takes place for GO. The comparison of the thermal properties of g-C₃N₄, g-C₃N₄ + Fe₂O₃, and g-C₃N₄ + Fe₂O₃ + GO revealed differences in mass losses and thermal transitions of the individual samples. In the thermogravimetric analysis of pure g-C₃N₄, an endothermic peak was observed at 108.3 °C, associated with a mass loss of -1.93%, likely caused by the release of water or other volatile substances. The main exothermic decomposition occurred with a mass loss of -75.28%, and the residual mass at 750.1 °C was 22.44%.

The addition of Fe₂O₃ caused a shift in the endothermic peak to 106.5 °C, with a slightly reduced initial mass loss of -1.83%. A significant exothermic peak was observed at 596.3 °C, accompanied by a mass loss of -76.47%. The residual mass was also lower (21.64% at 749.3 °C), which can be attributed to the oxidation of residual carbon species catalysed by Fe₂O₃.

The addition of graphene oxide (GO) led to further significant changes. The endothermic peak shifted to a lower temperature (76.4 °C), with the initial mass loss being the smallest (-1.38%). A new exothermic event was observed at 238.9 °C, associated with an additional mass loss of -7.08%, likely due to the decomposition of oxygen-containing functional groups in GO (epoxy, hydroxyl, carbonyl, and carboxyl groups). The main exothermic peak shifted to 599.1 °C, with a total mass loss of -68.94%, and the residual mass reached its lowest value (20.91% at 749.2 °C). The total exothermic energy of the mixture increased to 5383 J/g, indicating higher reactivity.

The presence of GO introduced a more complex thermal decomposition pathway, as evidenced by an intermediate step in the mass loss and a lower residual mass.

Overall, the comparison demonstrated that the composition of $g\text{-C}_3\text{N}_4 + \text{Fe}_2\text{O}_3 + \text{GO}$ exhibits the most complex decomposition and thermal response. The presence of Fe_2O_3 caused a significant exothermic peak, while the addition of GO resulted in a multiphase decomposition and increased exothermic energy. The lower residual mass in the GO-containing mixture confirms greater degradation of the organic component, likely due to interactions between GO and the other components. The results clearly indicate that the addition of GO and Fe_2O_3 alters the thermal behaviour of the entire system and enhances its reactivity.

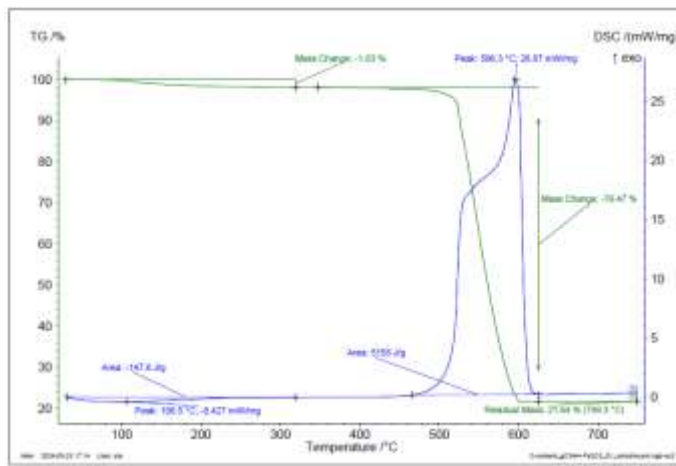


Figure 14. TGA and DSC analysis of $g\text{-C}_3\text{N}_4 + \text{Fe}_2\text{O}_3$.

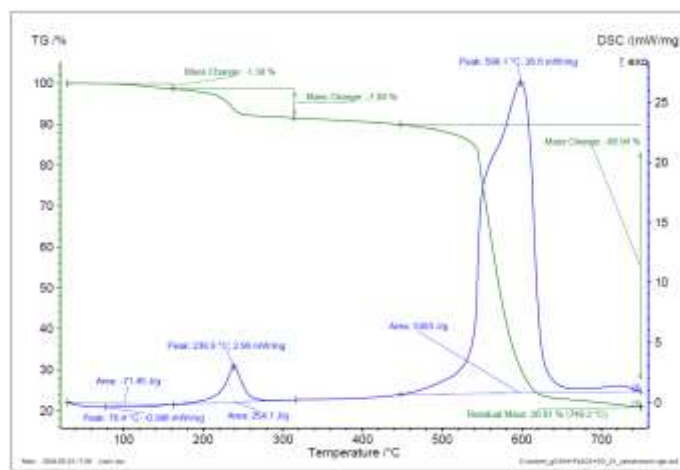


Figure 15. TGA and DSC analysis of $g\text{-C}_3\text{N}_4 + \text{Fe}_2\text{O}_3 + \text{GO}$.

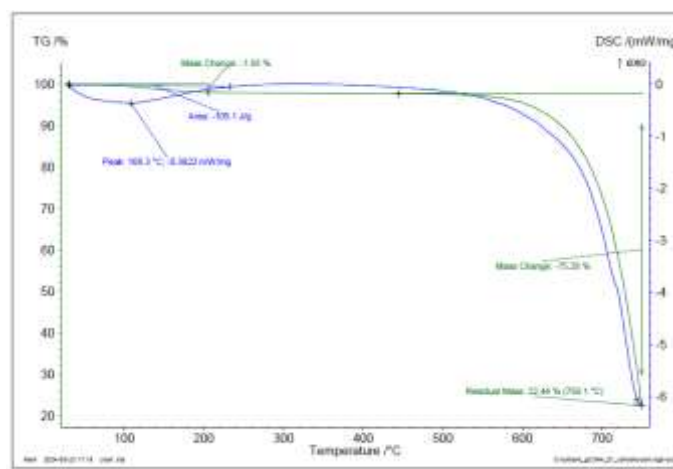


Figure 16. TGA and DSC analysis of $g\text{-C}_3\text{N}_4$.

3.2. Reaction with polyethylene – composite (g-C₃N₄, g-C₃N₄- PDA)

3.2.1. FTIR analysis

FTIR spectra of composites are presented on **Figures 17 and 18**.

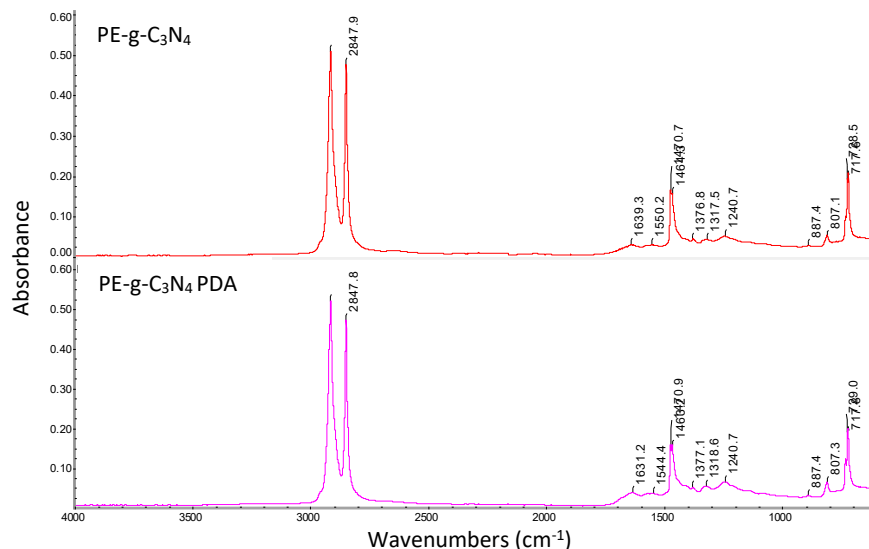


Figure 17. FTIR spectrum of PE-g-C₃N₄ and PE-g-C₃N₄ PDA films with determination of characteristic bands.

Characteristic bands for PE-g-C₃N₄ and PE-g-C₃N₄ PDA:

2915 cm⁻¹ vibration $\nu_{as}(\text{CH}_2)$, bond –CH₂

2848 cm⁻¹ vibration $\nu_s(\text{CH}_2)$, bond –CH₂

1471 cm⁻¹ vibration $\delta(\text{CH}_2)$, bond –CH₂

718 cm⁻¹ or 729 cm⁻¹ vibration $\rho(\text{CH}_2)$, bond –(CH₂)_n–

Additional vibrations of PE: 1464 cm⁻¹, 1377 cm⁻¹, 887 cm⁻¹, 718 cm⁻¹ or 729 cm⁻¹

Other bands:

1639 cm⁻¹, 1550 cm⁻¹ (or 1631 cm⁻¹, 1544 cm⁻¹ for PDA) vibration C=N

1377 cm⁻¹, 1318 cm⁻¹, 1241 cm⁻¹ vibration C–N

807 cm⁻¹ vibration of CN cycle

Figure 18 shows the FTIR spectrum of PP-g-C₃N₄ filament with the determined band character and the comparison of g-C₃N₄ spectra.

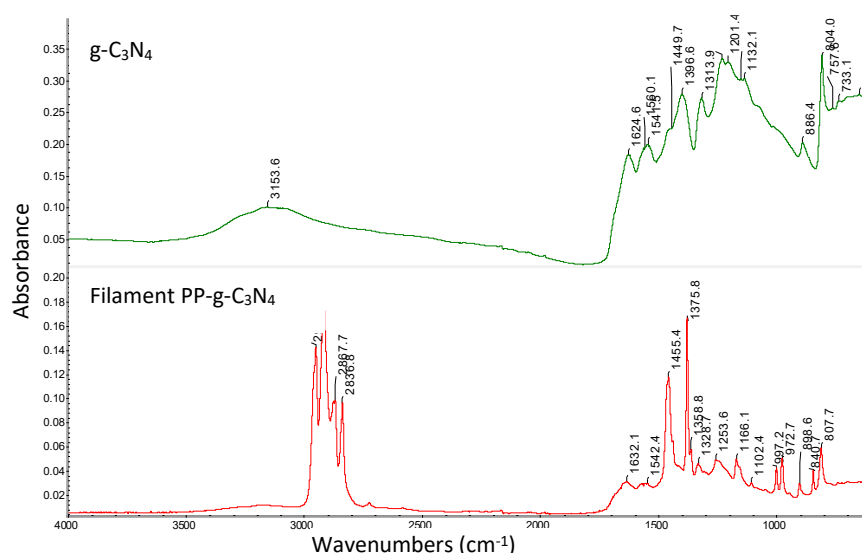


Figure 18. Comparison of FTIR spectra of initial g-C₃N₄ and PP g-C₃N₄ filament samples with determination of characteristic bands.

Characteristic bands for PP:

2949 cm⁻¹ vibration $\nu_{as}(\text{CH}_3)$, bond -CH₃

2916 cm⁻¹ vibration $\nu_{as}(\text{CH}_2)$, bond -CH₂

2876 cm⁻¹ vibration $\nu_s(\text{CH}_3)$, bond -CH₃ (not marked in the spectrum)

2868 cm⁻¹ vibration $\nu_s(\text{CH}_2)$, bond >CH-

2837 cm⁻¹ vibration $\nu_s(\text{CH})$, bond -CH₂

1455 cm⁻¹ vibration $\delta_{as}(\text{CH}_3)$, bond -CH₃ or vibration $\delta(\text{CH}_2)$, bond -CH₂

1376 cm⁻¹ vibration $\delta_s(\text{CH}_3)$, bond -CH₃

1166 cm⁻¹ vibration $\delta(\text{CH})$, bond -CH

997 cm⁻¹ vibration $\delta(\text{CH}_3)$, bond -CH₃

973 cm⁻¹ vibration δ for CH₃, CH₂ and CH

841 cm⁻¹ vibration δ for CH₂ and C-CH₃

808 cm⁻¹ chain vibration

1632 cm⁻¹, 1542 cm⁻¹ not determined, this might be the vibration of the g-C₃N₄ component

Additional vibrations of PP: 1329 cm⁻¹ (δCCH), 1254 cm⁻¹ (δCH_2), 1102 cm⁻¹, 899 cm⁻¹ (vibration C-C)

The FTIR spectra of the studied materials exhibit characteristic vibrations corresponding to their polymeric structures and the presence of graphitic carbon nitride (g-C₃N₄) (Table 1). For both PE-g-C₃N₄ and PE-g-C₃N₄ PDA, typical polyethylene bands appear at 2915 and 2848 cm⁻¹ for the asymmetric and symmetric stretching of -CH₂ groups, respectively, along with deformation vibrations at 1471 cm⁻¹ and rocking modes around 718 or 729 cm⁻¹. Additional PE-specific peaks are also observed at 1464/1463, 1377, and 887 cm⁻¹. Signals related to g-C₃N₄ include vibrations at 1639–1631 and 1550–1544 cm⁻¹, attributed to C=N stretching, and C-N vibrations around 1377, 1318–1319, and 1241 cm⁻¹. The presence of the triazine ring structure is

confirmed by a band near 807 cm^{-1} . In the case of PP-g-C₃N₄, characteristic polypropylene vibrations are present, such as –CH₃ and –CH₂ stretching at 2949, 2916, 2876, and 2868 cm^{-1} , and bending modes at 1455, 1376, and 1166 cm^{-1} . Additional PP-specific bands include those at 1329, 1254, and 1102 cm^{-1} . Notably, the PP-g-C₃N₄ spectrum also shows peaks at 1632 and 1542 cm^{-1} , which may correspond to the g-C₃N₄ component, indicating successful incorporation of the nitrogen-rich phase into the polymer matrix.

Table 1. Key FTIR absorption bands of g-C₃N₄-modified materials

| Wavenumber (cm ⁻¹) | Vibration Type | Bond/Group | Observed in |
|--------------------------------|---|--|---|
| 2949 | Asymmetric stretching (v _{as}) | –CH ₃ | PP-g-C ₃ N ₄ |
| 2915–2916 | Asymmetric stretching (v _{as}) | –CH ₂ | PE-g-C ₃ N ₄ , PE-g-C ₃ N ₄ PDA, PP-g-C ₃ N ₄ |
| 2876 | Symmetric stretching (v _s) | –CH ₃ | PP-g-C ₃ N ₄ |
| 2848–2868 | Symmetric stretching (v _s) | –CH ₂ / >CH– | All materials |
| 2837 | Symmetric stretching (v _s) | –CH (in –CH ₂) | PP-g-C ₃ N ₄ |
| 1631–1639 | Stretching (v) | C=N | All materials with C ₃ N ₄ |
| 1542–1550 | Stretching (v) | C=N | All materials with C ₃ N ₄ |
| 1471 | Bending (δ) | –CH ₂ | PE-g-C ₃ N ₄ , PE-g-C ₃ N ₄ PDA |
| 1455 | Asymmetric bending (δ _{as}) | –CH ₃ or –CH ₂ | PP-g-C ₃ N ₄ |
| 1376–1377 | Symmetric bending (δ _s) or stretching | –CH ₃ / C–N | All materials |
| 1318–1319 | Stretching (v) | C–N | PE-g-C ₃ N ₄ , PE-g-C ₃ N ₄ PDA |
| 1241 | Stretching (v) | C–N | PE-g-C ₃ N ₄ , PE-g-C ₃ N ₄ PDA |
| 1166 | Bending (δ) | –CH | PP-g-C ₃ N ₄ |
| 997–973 | Bending (δ) | –CH ₃ , –CH ₂ , –CH | PP-g-C ₃ N ₄ |
| 841 | Bending (δ) | –CH ₂ and C–CH ₃ | PP-g-C ₃ N ₄ |
| 807–808 | Ring vibration | Triazine ring (C ₃ N ₄) | All materials |

3.2.2. SEM analysis

The microstructure of LDPE+g-C₃N₄ film is presented in **Figure 19**. The film appears to be smooth with the visible lighter aggregates of different size and shape, **Figure 19A**. The estimated size/length of lighter spots is up to 10 μm . The higher magnification **Figure 19B and 19C** shows that the closest neighbourhood of spots is semi-disturbed. The film surface seems to be wrinkled similar to subtle waves (for the possible explanation see the notes below). The map of the elements distribution on the film surface is presented in **Figure 20**. Based on the registered maps it could be seen that the lighter spots are enriched in Nitrogen. The lack of Carbon at the same place is probably connected to the surface point-coverage by N. The microscopic images were taken with use of combined SE and BSE signals (SE+BSE). The heavier elements in BSE mode are represent in lighter shades of grey in comparison to less massive elements. In our research the Nitrogen ($M = 14\text{ g mol}^{-1}$) is slightly heavier than Carbon ($M = 12\text{ g mol}^{-1}$). Thus, based on the EDS maps and the SEM imaging techniques the lighter spots are quite certain connected to g-C₃N₄ particles.

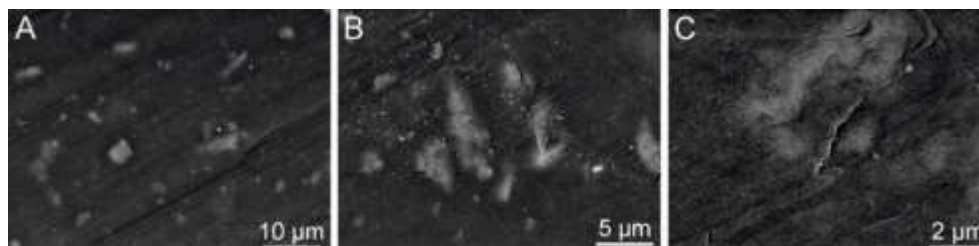


Figure 19. LDPE+g-C₃N₄; SEM: SE+BSE

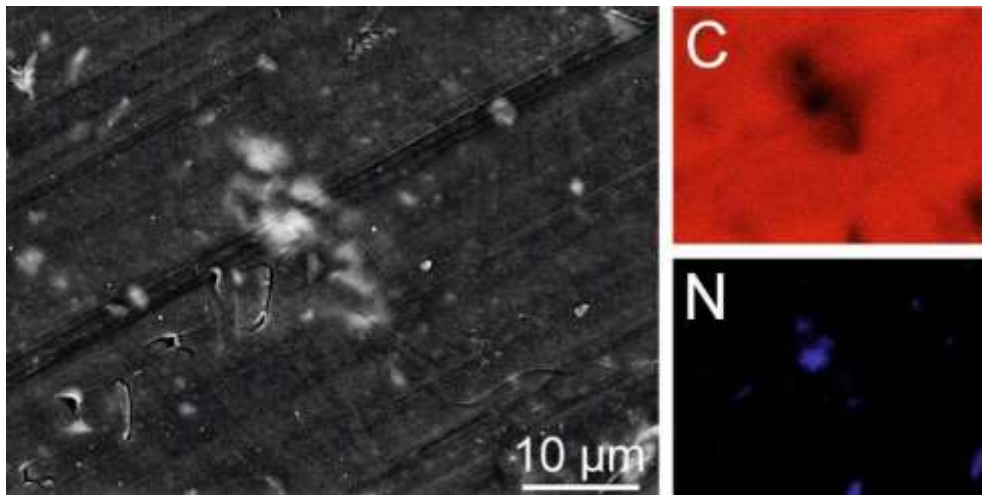


Figure 20. LDPE+g-C₃N₄ – EDS Mapping of C and N

3.2.3. TGA and DSC analysis

For the polyethylene-10% g-C₃N₄ composite, TGA and DSC analysis revealed its decomposition from 190 °C to 490 °C in the form of three interconnected exothermic effects with the maximums at 262°C, 352°C and the main one at 407 °C (**Figure 21**). At the end of the tested temperature range, the exothermic effect at 696 °C can still be identified – the decomposition of g-C₃N₄.

For the polyethylene 10% g-C₃N₄-PDA composite, the main exothermic effect with the maximum at 420 °C (**Figure 22**) was preceded by the associated exothermic effect with the maximum at 267 °C, and the resulting weight loss for this exothermic effect is minimal at about 0.5%. The decomposition of this polymer composite occurs in the temperature range of 240–490 °C, which is a slight shift by about 50 °C compared to non-doped g-C₃N₄. Here again the exothermic effect is at 688 °C – the decomposition of g-C₃N₄.

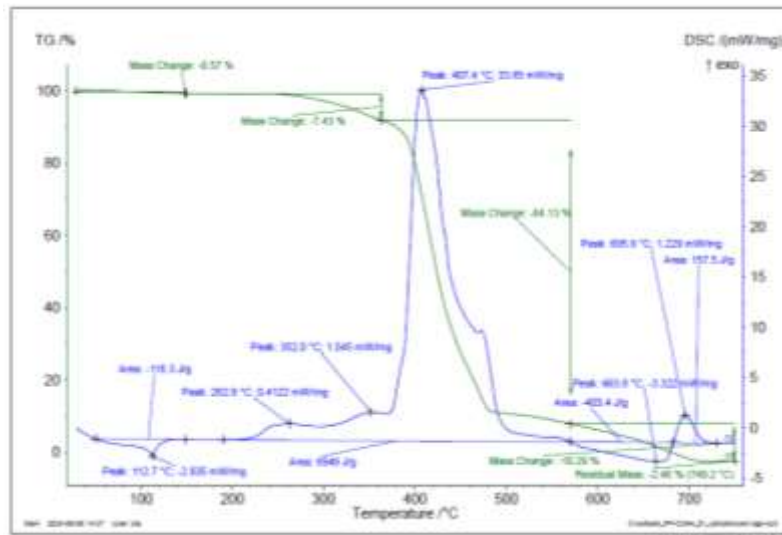


Figure 21. TGA and DSC analysis of g-C₃N₄-PE composite.

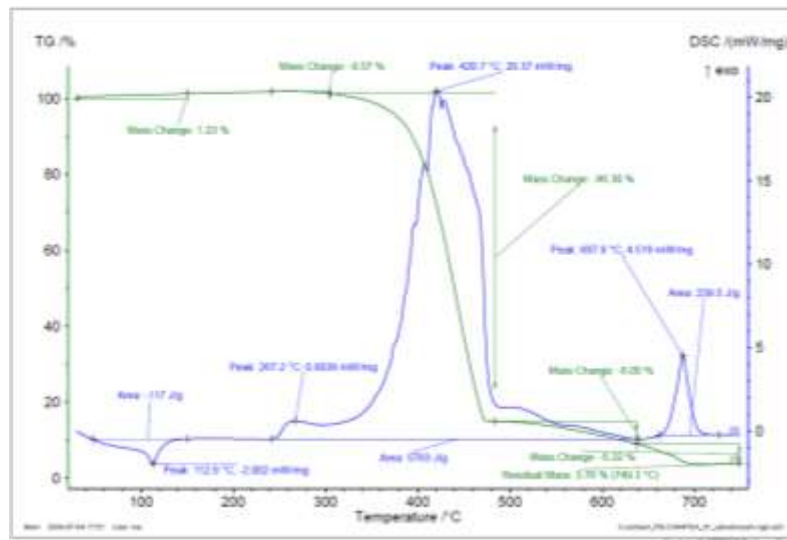


Figure 22. TGA and DSC analysis of g-C₃N₄-PDA-PE composite.

The thermal decomposition of the filament detected by TGA and DSC analysis, see **Figure 23**, associated with the weight loss of 90%, starts from the temperature of 240 °C with the exothermic effect with the maximum at 369 °C, and then the curve passes continuously through positive values into negative values, returns to positive values after about 300 °C, identifying the exothermic effect with the maximum at 698 °C in these values – the decomposition of g-C₃N₄.

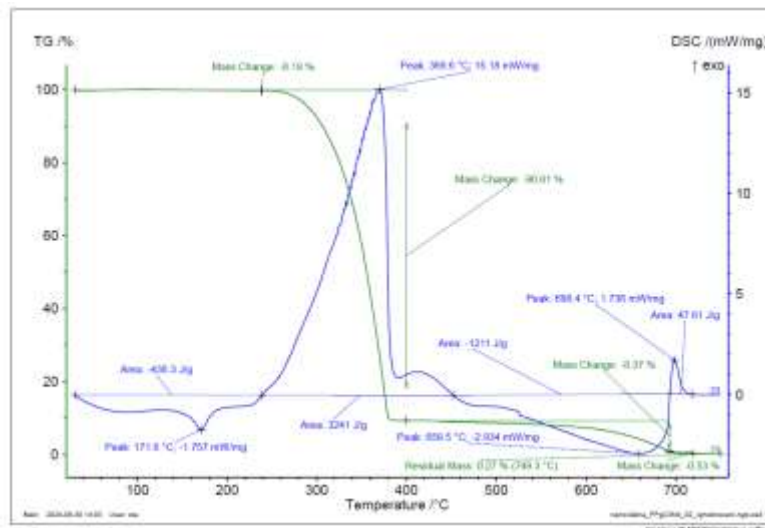


Figure 23. TGA and DSC analysis of PP-g-C₃N₄ filament.

3.3. Nanofibers prepared by DC and AC electrospinning

3.3.1. SEM analysis

SEM pictures of nanofibers prepared by DC and AX electrospinning are presented in **Figures 24-27**.

a) DC electrospinning - Nanospider™ (Elmarco, CZ)

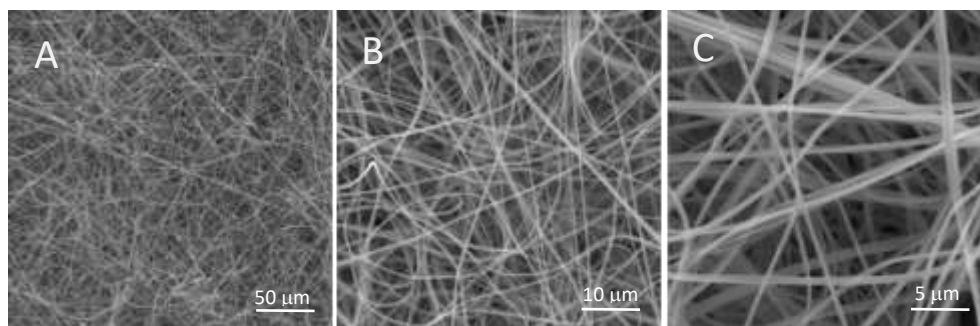


Figure 24. SEM analysis of PVB EL-DC nanofibers.

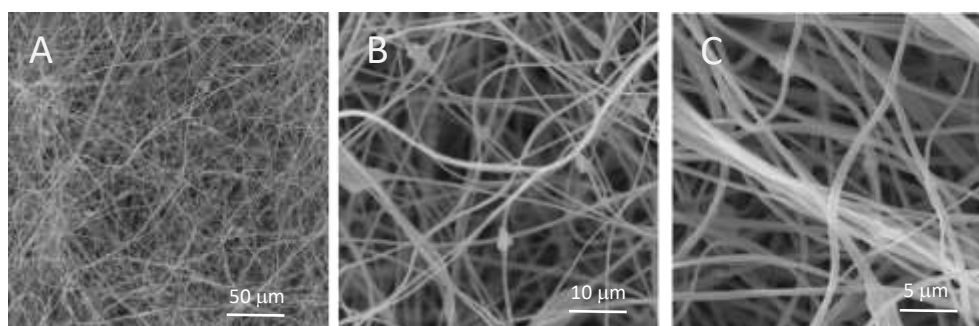


Figure 25. SEM analysis of PVB nanofiber with g-C₃N₄ EL-DC.

b) AC electrospinning – rod electrode

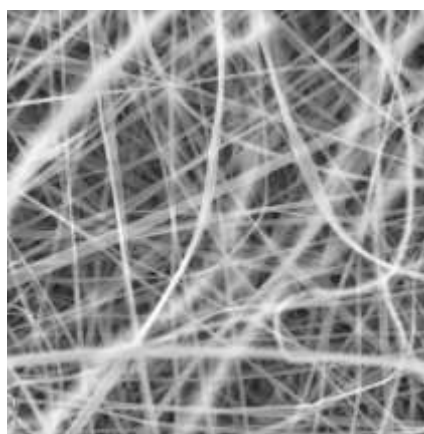


Figure 26. SEM analysis of PVB-EL-AC nanofibre.

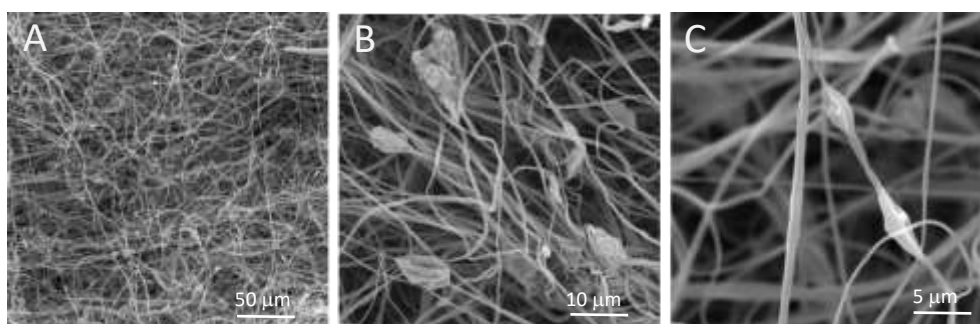


Figure 27. SEM analysis of PVB nanofibers with g-C₃N₄ EL-AC.

3.3.2. FTIR analysis

The nanofiber samples were subjected to FTIR, TGA and DSC analysis and the differences were also compared in relation to the spinning methodology (see FTIR samples in **Figures 28–30**).

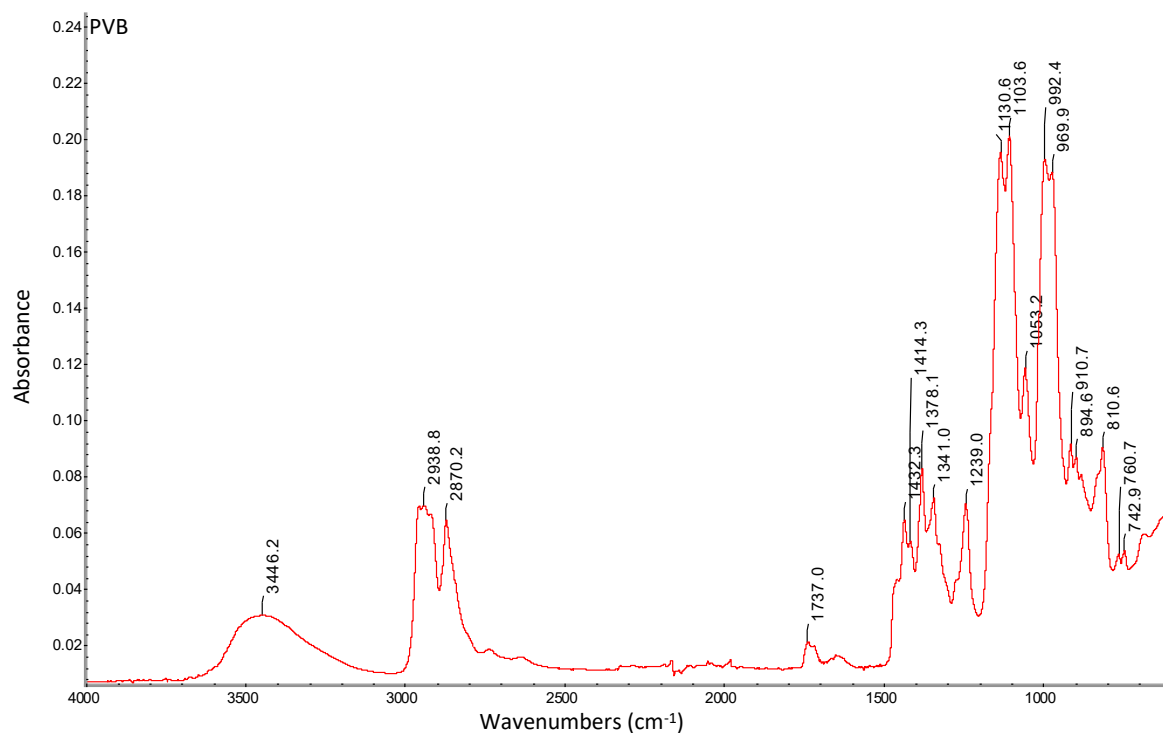


Figure 28. FTIR spectrum of initial PVB powder with determination of characteristic bands.

Description – Figure 28:

Characteristic bands for PVB:

3446 cm^{-1} vibration $\nu(\text{OH})$, bond $-\text{OH}$

2955 cm^{-1} vibration $\nu_{\text{as}}(\text{CH}_3)$, bond $-\text{CH}_3$ (not marked in the spectrum)

Between the vibrations of 2955 cm^{-1} and 2870 cm^{-1} , visible “peaks” of the vibrations of $-\text{CH}_2$ and $-\text{CH}$ bonds, e.g. 2939 cm^{-1}

2870 cm^{-1} vibration $\nu_{\text{s}}(\text{CH}_3)$, bond $-\text{CH}_3$

1737 cm^{-1} vibration $\nu(\text{C}=\text{O})$, aldehydes

1432 cm^{-1} , 1414 cm^{-1} , 1378 cm^{-1} , 1341 cm^{-1} , 1239 cm^{-1}

vibration $\delta(\text{CH}_2)$, bond $-\text{CH}_2$ or vibration $\delta(\text{CH}_3)$, bond $-\text{CH}_3$ or vibration $\delta(\text{COH})$

1131 cm^{-1} , 1104 cm^{-1} vibration $\nu(\text{COC})$

1053 cm^{-1} vibration $\nu(\text{CCO})$, primary alcohol

Additional vibrations of PVB: 992 cm^{-1} , 970 cm^{-1} , 911 cm^{-1} , 895 cm^{-1} , 878 cm^{-1} (not marked in the spectrum), 811 cm^{-1} , 761 cm^{-1} , 743 cm^{-1}

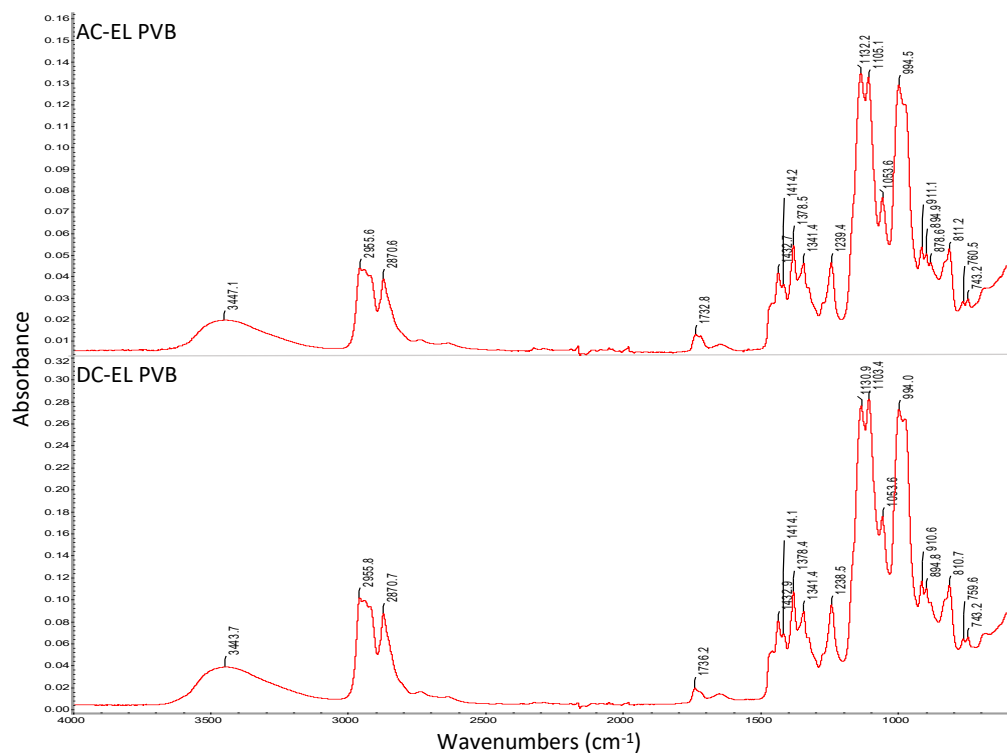


Figure 29. FTIR spectrum of pure PVB nanofibers with determination of characteristic AC and DC electrospinning bands (AC-EL and DC-EL).

Description – Figure 29 (AC-EL):

Characteristic bands for PVB:

3447 cm^{-1} vibration $\nu(\text{OH})$, bond $-\text{OH}$

2956 cm^{-1} vibration $\nu_{\text{as}}(\text{CH}_3)$, bond $-\text{CH}_3$

Between the vibrations of 2956 cm^{-1} and 2871 cm^{-1} , visible “peaks” of the vibrations of $-\text{CH}_2$ and $-\text{CH}$ bonds

2871 cm^{-1} vibration $\nu_{\text{s}}(\text{CH}_3)$, bond $-\text{CH}_3$

1733 cm^{-1} vibration $\nu(\text{C}=\text{O})$, aldehydes

1433 cm^{-1} , 1414 cm^{-1} , 1379 cm^{-1} , 1341 cm^{-1} , 1239 cm^{-1}

vibration $\delta(\text{CH}_2)$, bond $-\text{CH}_2$ or vibration $\delta(\text{CH}_3)$, bond $-\text{CH}_3$ or vibration $\delta(\text{COH})$

1132 cm^{-1} , 1105 cm^{-1} vibration $\nu(\text{COC})$

1054 cm^{-1} vibration $\nu(\text{CCO})$, primary alcohol

Additional vibrations of PVB: 995 cm^{-1} , 972 cm^{-1} (not marked in the spectrum), 911 cm^{-1} , 895 cm^{-1} , 879 cm^{-1} , 811 cm^{-1} , 761 cm^{-1} , 743 cm^{-1}

Description – Figure 29 (DC-EL):

Characteristic bands for PVB:

3444 cm^{-1} vibration $\nu(\text{OH})$, bond $-\text{OH}$

2956 cm^{-1} vibration $\nu_{\text{as}}(\text{CH}_3)$, bond $-\text{CH}_3$

Between the vibrations of 2956 cm^{-1} and 2871 cm^{-1} , visible “peaks” of the vibrations of $-\text{CH}_2$ and $-\text{CH}$ bonds:

2871 cm^{-1} vibration $\nu_{\text{s}}(\text{CH}_3)$, bond $-\text{CH}_3$

1736 cm^{-1} vibration $\nu(\text{C}=\text{O})$, aldehydes
 1433 cm^{-1} , 1414 cm^{-1} , 1378 cm^{-1} , 1341 cm^{-1} , 1239 cm^{-1}
 vibration $\delta(\text{CH}_2)$, bond $-\text{CH}_2$ or vibration $\delta(\text{CH}_3)$, bond $-\text{CH}_3$ or vibration $\delta(\text{COH})$
 1131 cm^{-1} , 1103 cm^{-1} vibration $\nu(\text{COC})$
 1054 cm^{-1} vibration $\nu(\text{CCO})$, primary alcohol
 Additional vibrations of PVB: 994 cm^{-1} , 911 cm^{-1} , 895 cm^{-1} , 811 cm^{-1} , 760 cm^{-1} , 743 cm^{-1}

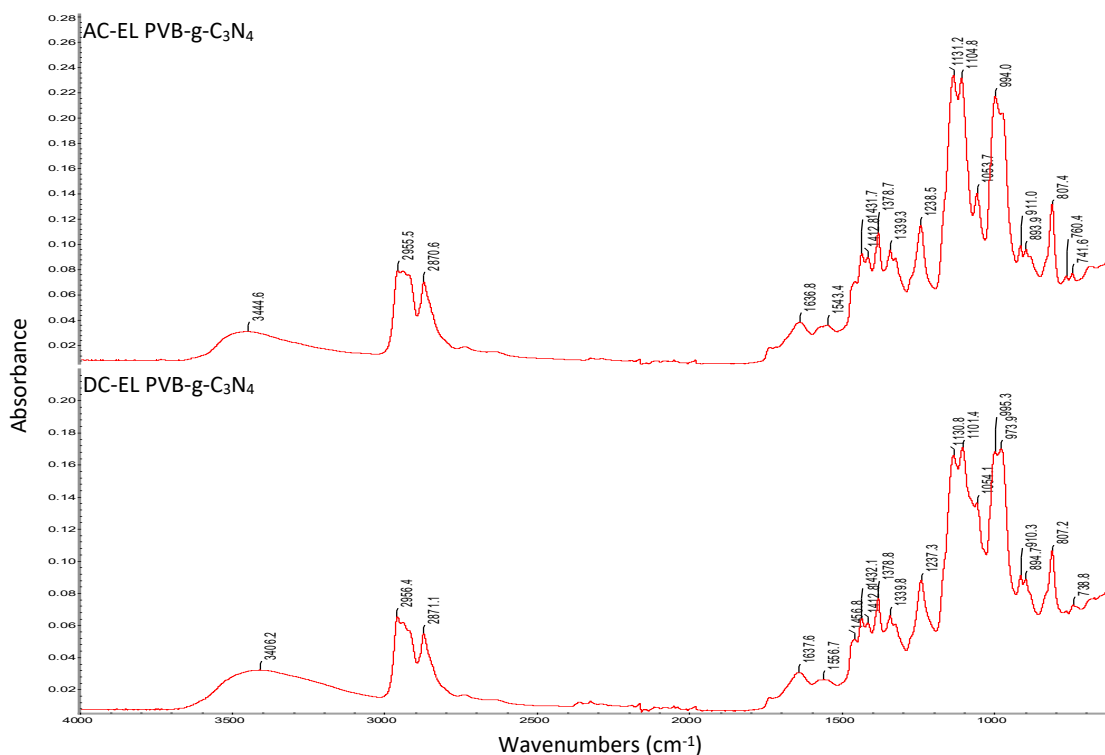


Figure 30. FTIR spectrum of nanofiber sample with PVB-g-C₃N₄ AC electrospinning (AC-EL), and PVB-g-C₃N₄ DC-EL nanofiber sample with determination of characteristic bands.

Description – Figure 30 (AC-EL):

3445 cm^{-1} vibration $\nu(\text{OH})$, bond $-\text{OH}$
 2956 cm^{-1} vibration $\nu_{\text{as}}(\text{CH}_3)$, bond $-\text{CH}_3$
 Between the vibrations of 2956 cm^{-1} and 2871 cm^{-1} , visible “peaks” of the vibrations of $-\text{CH}_2$ and $-\text{CH}$ bonds
 2871 cm^{-1} vibration $\nu_{\text{s}}(\text{CH}_3)$, bond $-\text{CH}_3$
 1432 cm^{-1} , 1413 cm^{-1} , 1379 cm^{-1} , 1339 cm^{-1} , 1239 cm^{-1}
 vibration $\delta(\text{CH}_2)$, bond $-\text{CH}_2$ or vibration $\delta(\text{CH}_3)$, bond $-\text{CH}_3$ or vibration $\delta(\text{COH})$
 1131 cm^{-1} , 1105 cm^{-1} vibration $\nu(\text{COC})$
 1054 cm^{-1} vibration $\nu(\text{CCO})$, primary alcohol
 Negligible band 1735 cm^{-1} for vibrations $\nu(\text{C}=\text{O})$, aldehydes
 Additional vibrations of PVB: 994 cm^{-1} , 911 cm^{-1} , 894 cm^{-1} , 807 cm^{-1} , 760 cm^{-1} , 742 cm^{-1}
 Other bands: 1637 cm^{-1} , 1543 cm^{-1} vibration $\text{C}=\text{N}$
 1432 cm^{-1} , 1413 cm^{-1} , 1379 cm^{-1} , 1339 cm^{-1} , 1239 cm^{-1}

The above vibrations or C-N vibrations

807 cm⁻¹ band for PVB or vibrations of the CN cycle

Description – Figure 30 (DC-EL):

3406 cm⁻¹ vibration $\nu(\text{OH})$, bond –OH

2956 cm⁻¹ vibration $\nu_{\text{as}}(\text{CH}_3)$, bond –CH₃

Between the vibrations of 2956 cm⁻¹ and 2871 cm⁻¹, visible “peaks” of the vibrations of –CH₂ and –CH bonds

2871 cm⁻¹ vibration $\nu_{\text{s}}(\text{CH}_3)$, bond –CH₃

1432 cm⁻¹, 1413 cm⁻¹, 1379 cm⁻¹, 1340 cm⁻¹, 1237 cm⁻¹

vibration $\delta(\text{CH}_2)$, bond –CH₂ or vibration $\delta(\text{CH}_3)$, bond –CH₃ or vibration $\delta(\text{COH})$

1131 cm⁻¹, 1101 cm⁻¹ vibration $\nu(\text{COC})$

1054 cm⁻¹ vibration $\nu(\text{CCO})$, primary alcohol

Additional vibrations of PVB: 995 cm⁻¹, 974 cm⁻¹, 910 cm⁻¹, 895 cm⁻¹, 807 cm⁻¹, 739 cm⁻¹

Other bands: 1638 cm⁻¹, 1557 cm⁻¹ vibration C=N

1432 cm⁻¹, 1413 cm⁻¹, 1379 cm⁻¹, 1340 cm⁻¹, 1237 cm⁻¹

The above vibrations or C-N vibrations

807 cm⁻¹ band for PVB or vibrations of the CN cycle

The measured FTIR spectra were from the initial graphitic carbon nitride g-C₃N₄, from g-C₃N₄-free polyvinyl butyral nanofibers fabricated by DC electrospinning. Further nanofiber spectra were already taken with the g-C₃N₄ composite, but using a different spinning technique.

The FTIR spectra of PVB powder and its composites reveal characteristic absorption bands associated with the polyvinyl butyral structure, along with signals indicating the presence of g-C₃N₄ in the modified materials (Table 2). All samples exhibit a broad –OH stretching band around 3444–3447 cm⁻¹, along with asymmetric and symmetric –CH₃ stretching vibrations at approximately 2955–2956 cm⁻¹ and 2870–2871 cm⁻¹, respectively. Additional peaks between these values correspond to –CH₂ and –CH vibrations. A notable $\nu(\text{C=O})$ vibration of aldehydes appears around 1733–1737 cm⁻¹ in unmodified PVB materials, although this band is significantly reduced or nearly absent in the PVB-C₃N₄ composites, suggesting interaction or consumption of carbonyl groups. Bending vibrations of –CH₂, –CH₃, and –COH appear consistently at 1432–1413, 1379–1340, and 1239–1237 cm⁻¹. Strong $\nu(\text{COC})$ and $\nu(\text{CCO})$ vibrations, typical of acetal and alcohol groups, are observed around 1131–1101 and 1053–1054 cm⁻¹, respectively. The presence of g-C₃N₄ in the AC-EL PVB-C₃N₄ and DC-EL PVB-C₃N₄ samples is confirmed by bands at approximately 1637–1638 and 1543–1557 cm⁻¹, attributed to C=N stretching, and additional vibrations in the fingerprint region related to C–N bonds and the triazine ring (e.g. 807 cm⁻¹). These spectra suggest successful incorporation of the g-C₃N₄ phase into the PVB matrix, accompanied by minor structural shifts in the polymer structure.

Table 2. Key FTIR bands of PVB-based materials.

| Wavenumber | Vibration Type | Bond/Group | Observed in |
|------------|---|------------------|-------------------------|
| 3444–3447 | Stretching (ν) | –OH | All PVB-based materials |
| 2955–2956 | Asymmetric stretching (ν_{as}) | –CH ₃ | All PVB-based materials |
| 2870–2871 | Symmetric stretching (ν_{s}) | –CH ₃ | All PVB-based materials |

| Wavenumber | Vibration Type | Bond/Group | Observed in |
|---------------|----------------------------|--|---|
| ~2939 (broad) | Stretching (ν) | –CH ₂ and –CH | All PVB-based materials |
| 1733–1737 | Stretching (ν) | C=O (aldehydes) | PVB, AC-EL PVB, DC-EL PVB (weakened in PVB-g-C ₃ N ₄) |
| 1432–1340 | Bending (δ) | –CH ₂ , –CH ₃ , –COH | All PVB-based materials |
| 1239–1237 | Bending (δ) | –COH | All PVB-based materials |
| 1131–1101 | Stretching (ν) | C–O–C (acetal group) | All PVB-based materials |
| 1053–1054 | Stretching (ν) | C–C–O (primary alcohol) | All PVB-based materials |
| 807 | Ring vibration or PVB band | Triazine ring | All PVB-g-C ₃ N ₄ materials |
| 1637–1638 | Stretching (ν) | C=N | AC-EL PVB-g-C ₃ N ₄ , DC-EL PVB-g-C ₃ N ₄ |
| 1543–1557 | Stretching (ν) | C=N | AC-EL PVB-g-C ₃ N ₄ , DC-EL PVB-g-C ₃ N ₄ |

Table 2. (Continued)

3.3.3. TGA and DSC analysis

The graphic carbon nitride decomposes with endothermic effect with the maximum at 748 °C, the beginning of the endothermic effect is at 565 °C, which immediately passes to the exothermic effect at 772°C (**Figure 31**). The nanofiber spun from polyvinyl butyral (PVB) by DC electrospinning decomposes over a wide temperature range from 225 °C to 600 °C with a continuous exothermic effect identified with six maximums at 331 °C, 386 °C, 414 °C, 495 °C, 520 °C and 534 °C in the energy range of 2-6 mW/mg (**Figure 32**). This composite, prepared by DC spinning, decomposes in the temperature range from 275 °C to 550 °C with the weight loss of 76% with a low heat flow compared to pure PVB – for comparison see **Figure 32** and **Figure 34**. In contrast, the exothermic effect was identified with a strong energy flow (17 mW mg⁻¹) with the maximum at 616 °C and the weight loss of 14% (**Figure 33**). A different spectrum from thermographic analysis was obtained from the PVB-g-C₃N₄ composite obtained by AC spinning (**Figure 35**). Two exothermic effects with maximums at 402 °C and 495 °C are separately identified in the spectrum, which pass to the endothermic effect with the maximum at 625 °C followed by the exothermic effect at 693 °C. The interaction between the composite and the polymer resulted, for example, in the decrease in maximum values for both the endothermic effect and the exothermic effect. The effect of the spinning method on the behaviour of composite nanofibre during thermal stress has been also shown. We assume suppression of, for example, g-C₃N₄ sublimation TGA and DSC of PVB powder is presented in **Figure 36**. For clarity, the affected spectra of the TGA and DSC analysis are shown in the following pyramid scheme (see **Figures A1** and **Figures A2** in Supplementary).

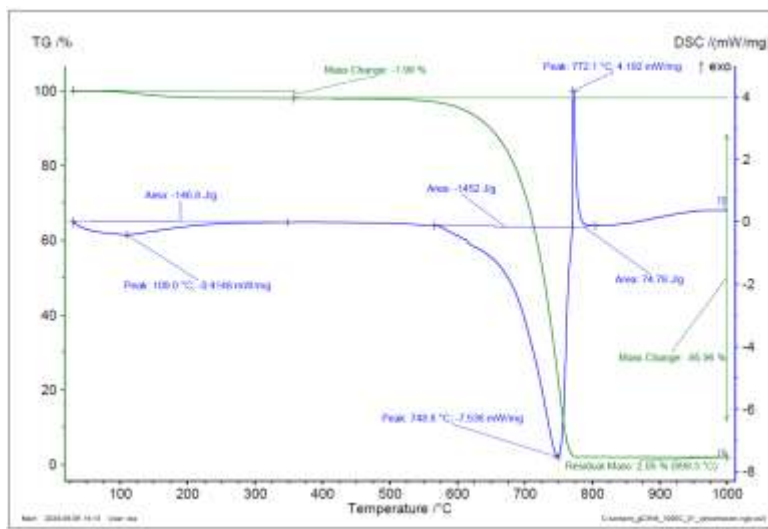


Figure 31. TGA and DSC analysis of g-C₃N₄ sample.

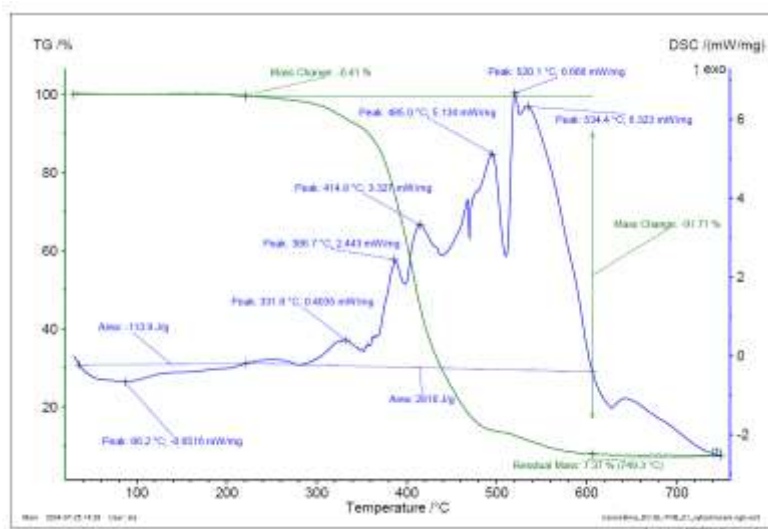


Figure 32. TGA and DSC analysis of PVB EL-DC nanofiber.

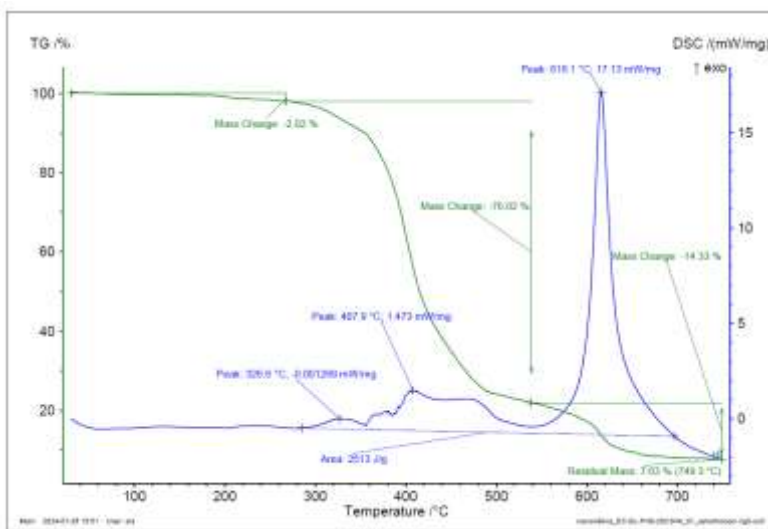


Figure 33. TGA and DSC analysis of PVB-g-C₃N₄ EL-DC nanofiber.

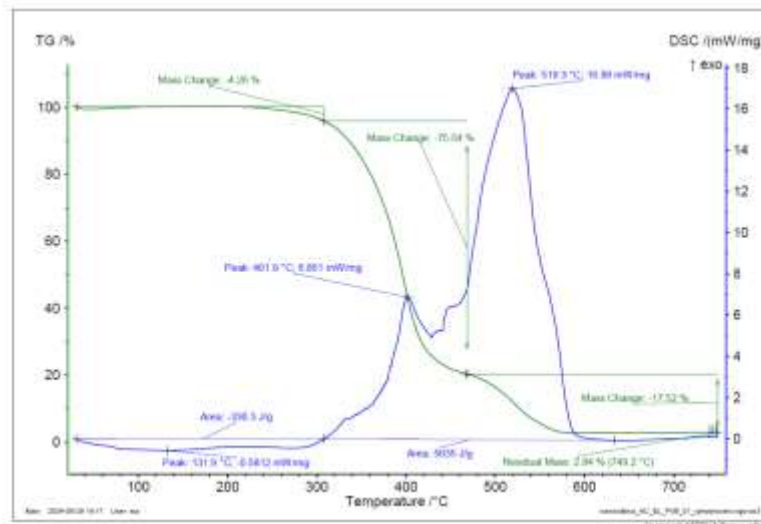


Figure 34. TGA and DSC analysis of PVB EL-AC nanofiber.

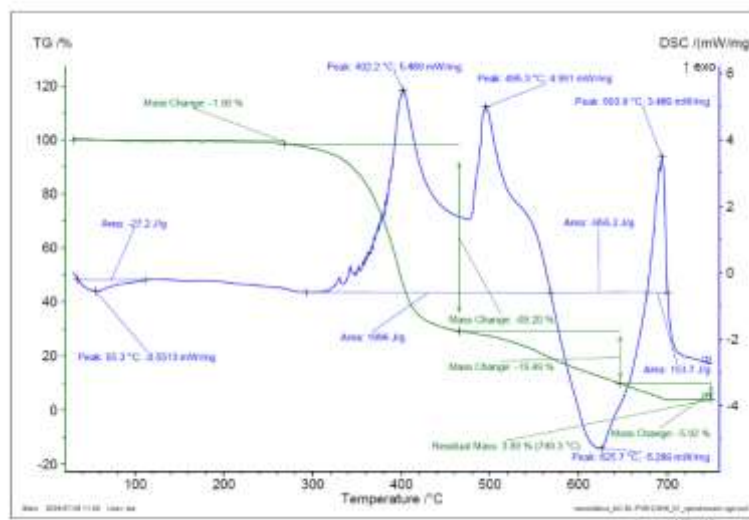


Figure 35. TGA and DSC analysis of PVB-g-C₃N₄-EL-AC nanofiber.

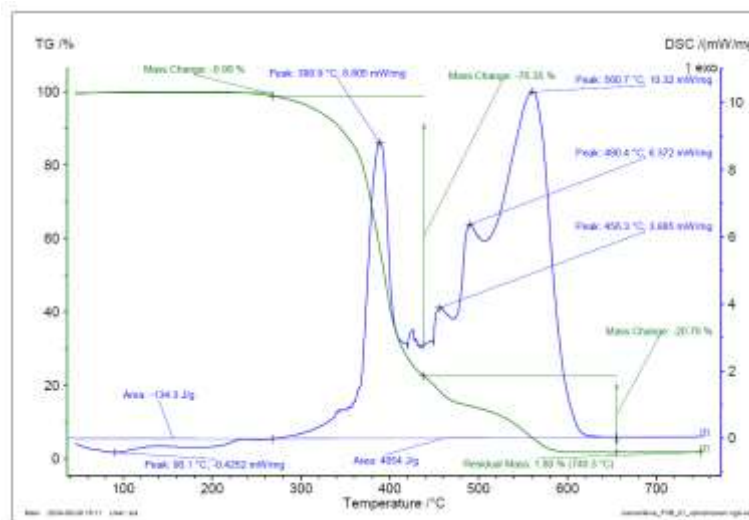


Figure 36. TGA and DSC of PVB powder.

4. Conclusion

The aim of this work was to investigate the thermal stability of g-C₃N₄ and its modifications. First, the preparation of g-C₃N₄ and further reactions with various modifications of GO (graphene oxide) and other

materials are described. The following section focuses on the description of electrospinning using direct and alternating current with attention to the differences between these fabrication techniques. The first part of the experimental results of the work focuses on doped g-C₃N₄ (GO, Fe₂O₃, H₂O₂, etc.) presented by FTIR analyses of the different materials and modifications, then SEM analyses using different magnifications are also presented, with clear differences in the structures of the different modifications. Finally, TGA analyses are described, the purpose of which was to test the response of the materials to thermal decomposition. The second part of the experiments is described in analogy to the first part, the only difference being the use and comparison of plastic composites (PP, PE, LDPE, PVB). FTIR analyses, SEM and TGA/DSC analyses are presented. FTIR spectroscopy confirmed the successful incorporation of g-C₃N₄ into the PVB matrix, as evidenced by characteristic C=N and triazine ring vibrations in the composite spectra. The observed shifts and reductions in specific absorption bands, particularly the diminished carbonyl signal, suggest chemical interactions between g-C₃N₄ and the polymer structure. These structural modifications indicate that the presence of g-C₃N₄ influences the molecular environment of PVB, potentially enhancing the composite's functional properties. Pure g-C₃N₄ exhibited a distinct endothermic decomposition peak at 748 °C, while PVB nanofibers decomposed over a broad temperature range with multiple exothermic transitions. The incorporation of g-C₃N₄ into PVB significantly altered the thermal decomposition profile, with the composite showing reduced weight loss and modified heat flow characteristics compared to pure PV. The main objective of this work was to modify the prepared g-C₃N₄ in such a way that the photocatalytic capabilities of this material and the prepared modifications can be tested in the planned follow-up experiments.

Author contributions

For research articles with several authors, a short paragraph specifying their individual contributions must be provided. The following statements should be used “Conceptualization, K.K.; methodology, K.K.; validation R.F. and Z.Z.; formal analysis, K.B.; investigation P.B.;E. K.K.; Z.S.; resources, J.T.; data curation, K.K.; writing—original draft preparation, K.K.; writing—review and editing, P.R.; visualization, K.K.; supervision, P.R.; All authors have read and agreed to the published version of the manuscript.” Please turn to the [CRediT taxonomy](#) for the term explanation. Authorship must be limited to those who have contributed substantially to the work reported.

Funding

This work was realized by using Large Research Infrastructure ENREGAT supported by the Ministry of Education, Youth and Sports of the Czech Republic (project No. LM2023056).

Acknowledgement

The authors express their gratitude to Martina Vráblová and Kamil Maciej Górecki for their contributions to the composition and quantification of this article.

Conflict of interest

The authors declare no conflict of interest.

References

1. Singh, P.; Srivastava, V. Recent advances in visible-light graphitic carbon nitride (g-C₃N₄) photocatalysts for chemical transformations. *RSC Adv.* 2022, 12, 18245–18265. doi: 10.1039/D2RA01797K.
2. Qamar, M.A.; Javed, M.; Shahid, S.; Shariq, M.; Fadhali, M.M.; Ali, S.K.; Khan, M.S. Synthesis and applications of graphitic carbon nitride (g-C₃N₄) based membranes for wastewater treatment: A critical review. *Heliyon* 2023, 9 (1), ISSN 2405-8440. doi:10.1016/j.heliyon.2022.e12685.

3. Chen, Y.; Lu, C. Graphitic carbon nitride nanomaterials for high-performance supercapacitors. *Carbon Neutralization* 2023, 2, 585–602. doi:10.1002/cnl2.87.
4. Miao, Z.; Wu, G.; Wang, Q.; Yang, J.; Wang, Z.; Yan, P.; Sun, P.; Lei, Y.; Mo, Z.; Xu, H. Recent advances in graphitic carbon nitride-based photocatalysts for solar-driven hydrogen production. *Mater. Rep. Energy* 2023, 3 (4), 100235. ISSN 2666-9358. doi:10.1016/j.matre.2023.100235.
5. Li, Y.; Zhu, S.; Liang, Y.; Li, Z.; Wu, S.; Chang, C.; Cui, Z. Synthesis of α -Fe₂O₃/g-C₃N₄ photocatalyst for high-efficiency water splitting under full light. *Mater. Des.* 2020, 109191. doi:10.1016/j.matdes.2020.109191.
6. Chen, M.M.A.; Li, M.; Qiu, X. Synthesis and modification strategies of g-C₃N₄ nanosheets for photocatalytic applications. *Adv. Powder Mater.* 2024, 3, doi:10.1016/j.apmate.2023.100150.
7. Li, X.; Huang, G.; Chen, X.; Huang, J.; Li, M.; Yin, J.; Li, Y. A review on graphitic carbon nitride (g-C₃N₄) based hybrid membranes for water and wastewater treatment. *Sci. Total Environ.* 2021, 792, 148462. doi:10.1016/j.scitotenv.2021.148462-
8. Vasiljević, J.; Jerman, I.; Simončič, B. Graphitic carbon nitride as a new sustainable photocatalyst for textile functionalization. *Polymers* 2021, 13 (15), 2568. <https://doi.org/10.3390/polym13152568>.
9. Zhang, M.; Yang, Y.; An, X.; Hou, L. A critical review of g-C₃N₄-based photocatalytic membrane for water purification. *Chem. Eng. J.* 2021, 412, 128663. doi:10.1016/j.cej.2021.128663.
10. Oluwole, A.; Khoza, P.; Olatunji, O.S. Synthesis and characterization of g-C₃N₄ doped with activated carbon (AC) prepared from grape leaf litters for the photocatalytic degradation of enrofloxacin in aqueous systems. *ChemistrySelect* 2022, 7 (45), e202203601.
11. Huang, J.; Hu, J.; Shi, Y.; Zeng, G.; Cheng, W.; Yu, H.; Yi, K. Evaluation of self-cleaning and photocatalytic properties of modified g-C₃N₄ based PVDF membranes driven by visible light. *J. Colloid Interface Sci.* 2019, doi:10.1016/j.jcis.2019.01.105.
12. Khurram, R.; Nisa, Z.; Javed, A.; Wang, Z.; Hussien, M. Synthesis and characterization of an Fe₂O₃-decorated g-C₃N₄ heterostructure for the photocatalytic removal of MO. *Molecules* 2022, 27, 1–18. doi:10.3390/molecules270414428.
13. Manickam, R.; Kokilavani, S.; Khan, S. Recent developments in architecturing the g-C₃N₄ based nanostructured photocatalysts: Synthesis, modifications and applications in water treatment. *Chemosphere* 2021, 291.
14. Rajeshwari, M.R.; Kokilavani, S.; Khan, S. Recent developments in architecturing the g-C₃N₄ based nanostructured photocatalysts: Synthesis, modifications and applications in water treatment. *Chemosphere* 2022, 291 (Pt 1), 132735.
15. Zhang, S.; Gu, P.; Ma, R.; Luo, C.; Wen, T.; Zhao, G.; Wang, X. Recent developments in fabrication and structure regulation of visible-light-driven g-C₃N₄-based photocatalysts towards water purification: A critical review. *Catal. Today* 2018, doi:10.1016/j.cattod.2018.09.013.
16. Ding, M.; Qu, Y.; Zhang, X.; Duan, L.; Li, X.; Lü, W. Reduced graphene oxide/g-C₃N₄ modified carbon fibers for high performance fiber supercapacitors. *New J. Chem.* 2021, 45 (2), 923–929. doi:10.1039/d0nj05072e.
17. Dong, J.; Zhang, Y.; Hussain, M.I.; Zhou, W.; Chen, Y.; Wang, L.N. g-C₃N₄: Properties, pore modifications, and photocatalytic applications. *Nanomaterials (Basel, Switzerland)* 2021, 12 (1), 121. <https://doi.org/10.3390/nano12010121>.
18. Bhandari, D.; Lakhani, P.; Modi, C. Graphitic carbon nitride (g-C₃N₄) as an emerging photocatalyst for sustainable environmental applications: A comprehensive review. *RSC Sustainability* 2023, 2, 10.1039/d3su00382e.
19. Roupčová, P. Monitoring of the ecotoxicity of the carbon based nanoparticles. Dissertation Thesis, VSB – Technical University of Ostrava, Faculty of Safety Engineering, 2018.
20. Bytešníková, Z.; Birgusová, E.; Pekárková, J.; Švec, P.; Richtera, L. A novel method for modification of poly(lactic acid) filament by graphene oxide for 3D print. In *Proceedings 15th International Conference on Nanomaterials - Research & Application; 2023; pp. 298–302. ISBN 978-80-88365-15-0. ISSN 2694-930X. doi: 10.37904/nanocon.2023.4799.*
21. Vilamová, Z.; Sampaio, M.J.; Svoboda, L.; Bednář, J.; Simonova, Z.; Dvorsky, R.; Silva, C.G.; Faria, J.L. Enhancing Photocatalytic g-C₃N₄/PVDF membranes through new insights into the preparation methods. *Polymer* 2024, 307, 127238. <https://doi.org/10.1016/j.polymer.2024.127238>
22. Vilamová, Z.; Czernek, P.; Zágora, J.; Svoboda, L.; Bednář, J.; Simonova, Z.; Placha, D.; Dvorsky, R. Fibrous PVDF membranes modified by anchored g-C₃N₄@GO composite with enhanced photocatalytic activity. *Appl. Surf. Sci.* 2024, 677, 161055. doi:10.1016/j.apsusc.2024.161055.
23. Wang, H.; Xu, Y.; Wei, Q. Preparation of bamboo-hat-shaped deposition of a poly(ethylene terephthalate) fiber web by melt-electrospinning. *Text. Res. J.* 2015, 85, 1838–1848.

24. Reneker, D. H.; Yarin, A. L.; Zussman, E.; Xu, H. Electrospinning of nanofibers from polymer solutions and melts. *Adv. Appl. Mech.* 2007, 41, 43–346.
25. Li, D.; Xia, Y. Electrospinning of nanofibers: reinventing the wheel? *Adv. Mater.* 2004, 16, 1151–1170.
26. Lomov, S. V.; Molnár, K. Compressibility of carbon fabrics with needleless electrospun PAN nanofibrous interleaves. *Express Polym. Lett.* 2015, 10, 25–35.
27. Nagy, Z. K.; Balogh, A.; Démuth, B.; Pataki, H.; Vigh, T.; Szabó, B.; Molnár, K.; Schmidt, B. T.; Horák, P.; Marosi, G.; Verreck, G.; Van Assche, I.; Brewster, M. E. High speed electrospinning for scaled-up production of amorphous solid dispersion of itraconazole. *Int. J. Pharm.* 2015, 480, 137–142.
28. Balogh, A.; Horváthová, T.; Fülöp, Z.; Loftsson, T.; Harasztos, A. H.; Marosi, G.; Nagy, Z. K. Electroblowing and electrospinning of fibrous diclofenac sodium-cyclodextrin complex-based reconstitution injection. *J. Drug Deliv. Sci. Technol.* 2015, 26, 28–34.
29. Pokorny, P.; Kostakova, E.; Sanetnik, F.; Mikes, P.; Chvojka, J.; Kalous, T.; Bilek, M.; Pejchar, K.; Valtera, J.; Lukas, D. Effective AC needleless and collectorless electrospinning for yarn production. *Phys. Chem. Chem. Phys.* 2014, 16, 26816–26822.
30. Lawson, C.; Stanishevsky, A.; Sivan, M.; Pokorny, P.; Lukáš, D. Rapid fabrication of poly(ϵ -caprolactone) nanofibers using needleless alternating current electrospinning. *J. Appl. Polym. Sci.* 2016, 133.
31. Balogh, A.; Farkas, B.; Verreck, G.; Mensch, J.; Borbás, E.; Nagy, B.; Marosi, G.; Nagy, Z. K. AC and DC electrospinning of hydroxypropylmethylcellulose with polyethylene oxides as secondary polymer for improved drug dissolution. *Int. J. Pharm.* 2016, 505, 159–166. doi:10.1016/j.ijpharm.2016.03.024.
32. Sun, B.; Long, Y. Z.; Zhang, H. D.; Li, M. M.; Duvail, J. L.; Jiang, X. Y.; Yin, H. L. Advances in three-dimensional nanofibrous macrostructures via electrospinning. *Prog. Polym. Sci.* 2014, 39, 862–890.
33. Darkwah, W.K.; Oswald, K.A. Photocatalytic applications of heterostructure graphitic carbon nitride: Pollutant degradation, hydrogen gas production (water splitting), and CO₂ reduction. *Nanoscale Res. Lett.* 2019, 14, 234. doi:10.1186/s11671-019-3070-3.

Appendix A

PVB POWDER and ITS SEM ANALYSIS

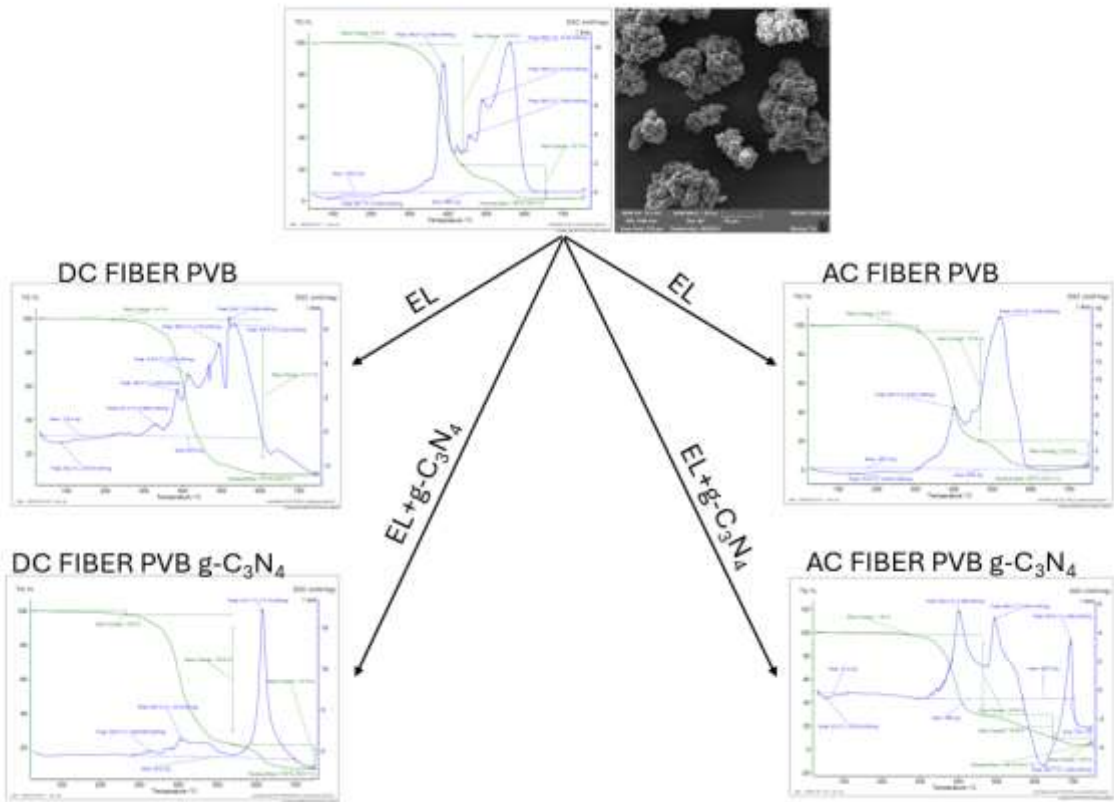


Figure A1. TGA and DSC analysis of initial PVB and prepared fibers without and with g-C₃N₄

PVB POWDER and ITS SEM ANALYSIS

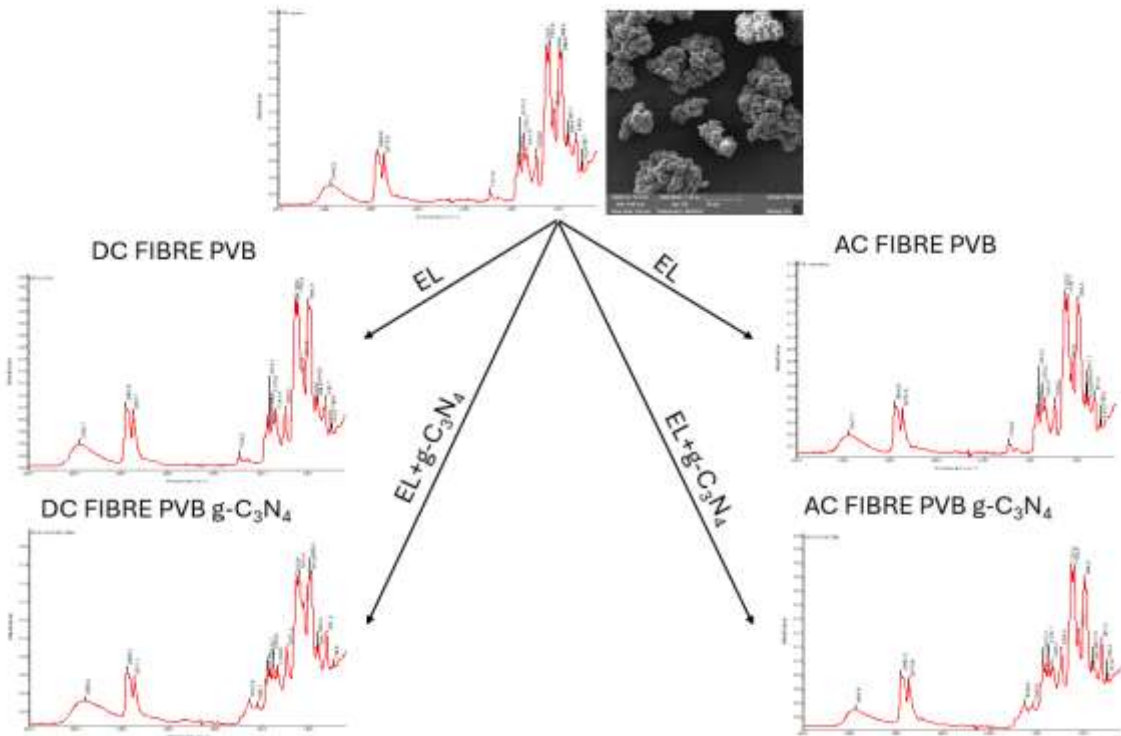


Figure A2. FTIR spectra of initial PVB and prepared fibers with and without g-C₃N₄

Findings after spectrum comparison could be found in **Tables A1** and **A2**.

Table A1. Temperature range required to achieve product distribution.

| Product name | Temperature [°C] | Residues [%] |
|---|------------------|--------------|
| PVB – powder | 380 | 1.8 |
| PVB – DC fiber | 390 | 7.3 |
| PVB – AC fiber | 326 | 2.8 |
| For the 1st and 3rd samples, the difference is 54°C | | |
| PVB DC fiber g-C ₃ N ₄ | 412 | 7.6 |
| PVB AC fiber g-C ₃ N ₄ | 460 | 3.8 |

The lowest temperature range where product decomposition occurs was measured for AC nanofiber, the initial powder has the value comparable to DC nanofiber. Both composites have a greater temperature range, up to 80 °C, compared to the initial powder.

Table. A2 Number of maximums for the product and thermal effect during decomposition.

| Product name | Number of maximums | Thermal effect [mW mg ⁻¹] |
|--|--------------------|---------------------------------------|
| PVB – powder | 4 | 29.382 |
| PVB – DC fiber | 6 | 24.296 |
| PVB – AC fiber | 2 | 23.831 |
| PVB DC fiber g-C ₃ N ₄ | 2 | 18.603 |
| PVB AC fiber g-C ₃ N ₄ | 3 | 8.680 |
| | +1* | |

* maximum during endothermic effect